

Accepted for publication in ApJ, October 2002

Imaging Spectroscopy for Extrasolar Planet Detection

William B. Sparks

Space Telescope Science Institute, 3700 San Martin Drive, Baltimore, MD 21218

and

Holland C. Ford

Dept. of Physics and Astronomy, The Johns Hopkins University, Baltimore, MD 21218

ABSTRACT

We propose that coronagraphic imaging in combination with moderate to high spectral resolution from the outset may prove more effective in both *detecting* extrasolar planets and characterizing them than a standard coronagraphic imaging approach. We envisage an integral-field spectrograph coupled to a coronagraph to produce a datacube of two space dimensions and one wavelength. For the idealised case where the spectrum of the star is well-known and unchanging across the field, we discuss the utility of cross-correlation to seek the extrasolar planet signal, and describe a mathematical approach to completely eliminate stray light from the host star (although not its Poisson noise). For the case where the PSF is dominated by diffraction and scattering effects, and comprises a multitude of speckles within an Airy pattern typical of a space-based observation, we turn the wavelength dependence of the PSF to advantage and present a general way to eliminate the contribution from the star while preserving both the flux and spectrum of the extrasolar planet. We call this method “spectral deconvolution”. We illustrate the dramatic gains by showing an idealized simulation that results in a $20\text{-}\sigma$ detection of a Jovian planet at 2 pc with a 2-m coronagraphic space telescope, even though the planet’s peak flux is only 1% that of the PSF wings of the host star. This scales to detection of a terrestrial extrasolar planet at 2 pc with an 8-m coronagraphic Terrestrial Planet Finder (TPF) in ~ 7 hr (or less with appropriate spatial filtering). Data on the spectral characteristics of the extrasolar planet and hence on its atmospheric constituents and possible biomarkers are obtained naturally as part of this process.

Subject headings: instrumentation: miscellaneous, methods: analytical, (stars:) planetary systems

arXiv:astro-ph/0209078v1 4 Sep 2002

1. Introduction

The detection of a large number of extrasolar planets and planetary systems through precision radial velocity surveys has revolutionized thinking on the frequency and characteristics of planets (Marcy and Butler 1998). It is now clear that extrasolar planets are common. Along with the discovery that life can exist and thrive in an extreme range of environments on Earth, this has given a strong stimulus and boost to the search for life elsewhere in the Universe. Major design studies have been undertaken to consider competing concepts for the Terrestrial Planet Finder (TPF) whose primary goal is to locate terrestrial extrasolar planets in the habitable zone (where liquid water may be present) and to characterize their atmospheres. It is thought that a combination of disequilibrium chemical processes will betray the presence of biological activity (Woolf and Angel 1998, see also <http://tpf.jpl.nasa.gov>).

Because of the faintness of planets, it has generally been assumed that characterization of Earth-like planets will be carried out at low spectral resolution. This maximizes the number of photons from the planet, per spectral resolution element, and allows the use of broad, deep molecular absorption bands to probe the atmosphere and to seek evidence of life (Kasting 1996, Woolf and Angel 1998, Schindler, Trent & Kasting 2000, Des Marais et al 2001). Here, we consider use of higher spectral resolution observations from the outset, although retaining the imaging context. The methods described will still work, however, to varying degrees at low resolution. Allowing ourselves to consider high resolution enables us to explore more novel approaches and understand some of the basic dependencies.

High spectral resolution observations have of course been obtained for the ground-breaking precision radial velocity measurements, and in addition high spectral resolution searches have been performed in order to attempt detection of extrasolar planets through the reflection of stellar photospheric emission, coupled to sophisticated numerical methods (Collier Cameron et al 2002). Detection of planetary atmospheres with high signal-to-noise transit spectroscopy has been both proposed and observed (Brown 2001, Charbonneau et al. 2002).

Classically, direct imaging of faint companions to bright stars has been carried out with coronagraphic observation. There has been a great deal of work devoted to improving the performance of coronagraphs with a multitude of analogue methods and data analysis techniques (e.g. Roddier & Roddier 1997, Rouan et al 2000, Spergel and Kasdin 2001; Kuchner & Traub 2002 and many others). Other approaches include manipulation of speckle patterns to reduce PSF haloes or recognize planetary signatures within the speckle noise, including the dark-speckle coronagraph (Boccaletti et al 1998) and the use of dichroics and differencing of speckle images (Racine et al. 1999, Marois et al 2000).

Our goal here is to detect and image extrasolar planets directly, that is separated from their host star, through photons reflected or emitted from their surface or atmosphere. The concept is to use a coronagraph together with integral-field spectroscopy (e.g. Bacon et al 1995). Recognition of the planetary spectrum within the multiple spectra into which the image is divided may be achieved using pattern recognition techniques or by manipulation of the stray light of the host star with the goal of eliminating it. The process can be aided by the orbital velocity of the planet which displaces its spectrum in wavelength from that of the star. The concepts outlined may be applicable to either space or ground-based observation.

Firstly we consider the case where the spectrum of the star is well-known and consistent across the field of view (i.e. spatially invariant; the same at all points of interest in its PSF). In § 3.1 we explore the statistical properties of straightforward cross-correlation of the spectra using a (matched) template. We show the trade-space between signal-to-noise (S/N) and rejection of stray light from the host star. In § 3.2 we present a mathematical approach which ensures *complete* elimination of stray light from the host star. By using Gram-Schmidt orthonormalization we show that the S/N of the correlation functions may be preserved while offering formally complete rejection of the host star light. In the absence of a matched template, analysis of variance methods, § 3.3, may be used to provide information on whether there are multiple spectroscopic components (i.e. planets or other companions) present. We develop spectral templates and idealized simulations for these concepts, which are more applicable to ground-based observation, in § 4.

In § 5.0 we discuss the alternate case that the PSF of the coronagraphic observation is dominated by diffraction, or diffraction plus scattering, and introduce the concept of “spectral deconvolution”. This situation is likely to apply to space-based observation, primarily, although there may be some ground-based opportunities using adaptive optics. We use the wavelength dependence of the PSF to advantage. By changing the image scale inversely to the wavelength the PSF is transformed into a simple, slowly varying function that can be removed e.g. by fitting low order polynomials as a function of wavelength. The extrasolar planet on the other hand is moved radially in the datacube by this process, and hence becomes a high frequency component which is ignored by the starlight rejection procedure. Reconstruction of the subtracted datacube back onto the original spatial scale and summation along the spectral dimension reveals the extrasolar planet signal. This method may prove exceptionally powerful and allows essentially *an ideal Poisson-noise limited imaging detection, which simultaneously provides a spectrum of the extrasolar planet*. In § 6, we speculate on future directions a spectroscopic approach might take, and § 7 summarizes our conclusions.

2. Concept

Collier Cameron et al (1999), Collier Cameron et al (2002) have utilized sophisticated pattern recognition techniques to place stringent limits on the contribution from a planet to the integrated light of a star hosting an extrasolar planet. Tonry & Davis (1979) describe the Fourier theory of cross-correlating a spectrum with a template and the associated error analysis for finding the (redshift) peak and (velocity dispersion) width. Here, we use elementary concepts involving spectroscopy not only to characterize extrasolar planets, but also to assess their utility in the detection process itself.

A standard instrumental approach is to obtain an image of the field of view which presumably contains a bright star and very faint nearby planet, perhaps a factor 10^9 or 10^{10} times fainter. Suppression of the starlight may be achieved through a variety of techniques, most commonly using an apodized coronagraph. Observation through several filters yields information on the flux distribution of the planet with wavelength, and hence its characteristics.

Now suppose we are presented with a similar field of view, but rather than integrate each portion of the image to measure the total flux from that region, or pixel, instead we disperse the light in each pixel using an integral-field spectrograph. We then explore the resulting datacube of two space dimensions and one spectral dimension to seek evidence of the extrasolar planet.

Temporal changes in spatial PSF structure may be accommodated since we envisage both spatial and spectral multiplexing. For long ground-based integrations, we expect rapid fluctuations from the constantly changing speckle pattern to average out in the spectral dimension. To approach the idealized case of a spatially invariant spectrum, further low order filtering of the spectra may be required. Experimentation with actual coronagraphs and actual integral field spectrographs would be invaluable in making a determination of the degree to which such an idealized situation may be approached in practice. For space based observation where PSFs are much more stable, the techniques of § 5 are more general and likely to be more easily applied than the pattern recognition methods described in the earlier sections, although over a limited wavelength range or close to the host star they may be useful. While we develop the ideas using both spatial and spectral multiplexing, either of these may be relaxed at the cost of implicitly imposing higher stability demands on the optical system, and additional exposure time to build up the datacube.

We assume that the dominant noise is the photon noise of the host star, i.e. that the detector noise is negligible. We are assuming that the planet is faint and therefore that the photon budget is dominated by residual light from the host star. If there are S_0 photons from

the star in a particular pixel, there are $\approx S_0/(Nn_{exp})$ photons for each of N spectral elements and n_{exp} exposures, hence this assumption requires $S_0 > Nn_{exp}\sigma_R^2$ if the detector readnoise is σ_R . For example, in the simulation of § 5 below, $S_0 \sim 9 \times 10^5$, $N \sim 600$ so the requirement is $\sigma_R < 38/\sqrt{n_{exp}}$. For a readnoise of, say, 4 photons, we could take 100 exposures and satisfy the constraint.

There is an analogy to the principal of “do no harm”. By ignoring the spectral dispersion of the light from each pixel, in our idealized configuration we simply recover the undispersed coronagraphic observation. That is, if we add all the counts in each spectrum, we obtain the flux at that pixel. This represents the best imaging detection limits currently (and in the near future) achievable. Yet, with the additional spectral dimension we may be able to achieve greatly improved rejection of contaminating starlight, knowledge of the extrasolar planet’s velocity and kinematics, and knowledge of its atmospheric characteristics, all with the *initial discovery* observation.

The first part of the discussion (§ 3 and § 4) considers the use of pattern recognition techniques to extract information on the faint extrasolar planet signal within the noisy spectrum under the assumption that the spectra of the residual light from the host star are the same everywhere in the field of view. There is a vast array of signal processing and pattern recognition techniques that could be brought to bear on such a dataset. To gain insight into some of the fundamental dependencies, however, we explore simple cross-correlation of the spectra with a matched template that has the same shape and structure as the target sought. The amplitude of the cross-correlation functions, as we show, depends on essentially two parameters: (i) the total flux from the extrasolar planet relative to the noise and (ii) the degree of structure, or variance, of the template. We extend the analysis to a general analysis of variance, and conclude this part of the discussion with a technique related to cross-correlation whereby template spectra are constructed that closely match the extrasolar planet’s spectrum but which are mathematically orthogonal to the stellar spectrum. Cross-correlation with such a template in the idealized case fully eliminates stray stellar light, although not the photon noise from that stray light.

The second part of the discussion (§ 5) offers a completely different way to remove the stray stellar light for the case where we have strong wavelength dependent diffraction limited PSFs, e.g. such as those obtained with space-based observation. The results of this procedure are *both* a Poisson limited image of the extrasolar planet and, from the outset, its spectrum, irrespective of the nature of that spectrum.

3. Correlation and Variance Methods: Theory and Error Analysis

3.1. Cross-correlation with matched template

If the planet has a grey, uniform albedo and isotropic scattering phase function, then the planet’s spectrum is the same as that of the stellar photosphere, many orders of magnitude weaker, and shifted in velocity by the planet’s orbital motion. If we are searching for a specific type of extrasolar planet, such as a terrestrial planet with strong molecular absorption features in the near infrared, or a Jovian planet with deep methane troughs, we may optimize the search by providing a template whose shape matches what we seek. We present a variety of templates in § 4, below. Eventually, to pursue this approach, one would build a library of spectra for comparison based on a mix of theory, modelling and observation.

Now consider a pixel in a coronagraphic image of a star and suppose there is a contribution to the signal from an extrasolar planet at that location. Let the total flux from the star in the (single) pixel and within the spectral window be S_0 and that of the planet be s_p . That is, S_0 is the portion of host star flux falling into a single pixel at some location in a coronagraphic image (not the total flux of the star over the whole image). Define a stellar template (spectrum) T such that $\int T(\lambda)d\log\lambda = 1.0$ and $T > 0.0$ everywhere (i.e. there are no regions of negative flux). Since we will sample the spectrum with quantized detector pixels, we will use a summation version of this, hence $\sum_i T_i = 1.0$ where T_i is $T(\lambda_i)$ the template at the i -th wavelength λ_i . That is, this template is normalized as a probability density function, and sampled on a logarithmically uniform grid.

The planet will have a spectrum similar in part to that of the star, since it shines by reflected starlight, modified by the albedo of the planet as a function of wavelength, by any absorption features in the planet’s atmosphere (through which the reflected light passes twice), by any intrinsic emission features, such as aurora, dayglow and nightglow, and shifted by the velocity of the planet. Let the probability density template t of the planet as a function of (logarithm) wavelength be t_i , also such that $\sum_i t_i = 1.0$.

We will use other versions of the templates. \hat{T} is a zero-mean version of T ; i.e. $\hat{T} = T - 1/N$ where N is the number of points in the spectrum. Also we define $T' = T \times N$; T' is such that $T' > 0$ everywhere and $\langle T' \rangle = 1.0$. It is simply the template obtained by normalizing the spectrum to have an average value of unity across the wavelength of interest. We define \hat{t} and t' in a similar way. In § 3.2, we define a norm, $\|x\| \equiv \sqrt{\sum_i x_i^2}$ and “normalized” zero-mean template $\tilde{T} = \hat{T}/\|T\|$.

Strictly speaking in the treatment of photon statistics we should use photon-weighted templates. However, over the wavelength ranges we adopt, the photon weighting is relatively

flat, and our detector is hypothetical. Therefore in our simulations, to avoid difficulty with end-effects and to focus on the influence of extrasolar planet atmospheric spectral features, we will deal with continuum normalized spectra. In practice, we may very well need to filter out low order terms that are irrelevant to the important aspects of the correlation functions and which may remain for a variety of practical reasons.

The total (undispersed) signal falling at a given single spatial pixel is, in photons, $S = S_0 + s_p$. A spectrum of this total flux may be expressed as:

$$S_i \equiv S(\lambda_i) = S_0.T_i + \epsilon_i + s_p.t_i$$

where ϵ_i is the photon shot noise from the star at wavelength λ_i , and the index i runs 1 to N for N sample points or wavelengths in each spectrum, and units are photons for S_i , S_0 , s_p , ϵ_i with T_i and t_i dimensionless. That is $S = \sum S_i$. We presume that there is some means to estimate the spatial shape and flux of the stellar PSF, either empirical or theoretical, and we will attempt to subtract this estimate of the host star PSF from the observation. The estimate of the true flux S_0 will in error by a fractional amount δ given by $S(\text{estimate}) = S_0(1 + \delta)$. Then consider the difference spectrum

$$\begin{aligned} d_i &= S_i - S_0(1 + \delta)T_i \\ d_i &= \epsilon_i + s_p.t_i - S_0.\delta.T_i \end{aligned} \tag{1}$$

where d_i is in photons, the index i corresponds to spectral dimension and, as above, ϵ_i is the noise and units are photons.

It is the difference spectrum d_i that we cross-correlate with the zero-mean template of the planet \hat{t} . Let the cross-correlation function c_j be given by

$$c_j \equiv \sum_i d_i \hat{t}_{i-j} = \sum_i \epsilon_i \hat{t}_{i-j} + s_p. \sum_i t_i \hat{t}_{i-j} - S_0.\delta. \sum_i T_i \hat{t}_{i-j} \tag{2}$$

Each of the terms in equation (2) has a different physical meaning and each contributes to detection capability. In the following subsections, we look at each term individually to understand its importance.

3.1.1. Signal from the Planet

The second term of Equ. (2) represents the signal from the planet. When the template is cross-correlated in the wavelength dimension with the signal, the value at the zero offset

position (i.e. “on” the planet) from the second term is

$$c_0 = s_p \sum_i t_i \hat{t}_i = s_p \sum_i (\hat{t}_i + 1/N) \hat{t}_i$$

$$c_0 = s_p \sum_i \hat{t}_i^2 \tag{3}$$

since $\sum_i \hat{t}_i = 0$ by definition.

We will also make use of the identity $\sum_i \hat{t}_i^2 = \sigma^2(t')/N$, where $\sigma(t')$ is the standard deviation of the template normalized to have unit mean in the region of study. This leads to $c_0 = (s_p/N)\sigma^2(t')$ for the “signal”. The t' (unit mean) template is the most straightforward to derive observationally, and its standard deviation offers an intuitive description of the degree of structure in the template.

3.1.2. Photon statistics and S/N

The first term of Equ. (2) is the photon shot noise from the host star, and at the correlation peak, from this first term, $c_0 = \sum_i \epsilon_i \hat{t}_i$. If there are S_0 photons from the star in the pixel, there are $S_i \approx S_0 T_i$ photons in spectral pixel i , and the expected dispersion per pixel from Poisson statistics is therefore $\sigma_i \approx \sqrt{S_0 T_i}$. Hence, the variance of the cross-correlation function at peak due to shot noise from the star is $E(c_0^2) = E((\sum_i \epsilon_i \hat{t}_i)^2)$ where E denotes expected value. It follows that $\sigma_{c_0}^2 \equiv E(c_0^2) = \sum_i \hat{t}_i^2 E(\epsilon_i^2)$ since the expected value of the cross terms, $E(\epsilon_i \epsilon_j)$, is zero due to the independence of ϵ_i and ϵ_j , and hence, since $E(\epsilon_i^2) = \sigma_i^2$ by definition,

$$\sigma_{c_0}^2 = \sum_i \hat{t}_i^2 S_0 T_i$$

$$\sigma_{c_0}^2 = S_0 \sum_i (\hat{T}_i + \frac{1}{N}) \hat{t}_i^2 \tag{4}$$

(where, again, the ‘hat’ symbol refers to a zero mean template). The latter term, $1/N$, is independent of the shape of the stellar template and dominates over the former, \hat{T}_i , for the cases we studied.

Combining equations (3) (signal) and (4) (noise), and using the identity mentioned in the previous section, we derive the S/N of the correlation peak due to photon statistics from the host star:

$$S/N = \frac{s_p}{\sqrt{S_0}} \frac{\sum_i \hat{t}_i^2}{\sqrt{\sum_i \hat{T}_i \hat{t}_i^2 + \sum_i \hat{t}_i^2/N}}$$

$$S/N = \frac{s_p}{\sqrt{S_0}} \times \sigma \times \frac{1}{\sqrt{1+f}} \quad (5)$$

where $\sigma \equiv \sigma(t')$ is the standard deviation of the unit-mean template and $f = \sum_i \hat{T}_i \hat{t}_i^2 / \sum_i \hat{t}_i^2$ which is a small quantity, for the cases we studied.

In words, the signal-to-noise S/N of the peak of the correlation function for a matched template is approximately the S/N of the direct image times the standard deviation σ of the template in its unit-mean form. To illustrate, the extreme situation is one where all the flux comes from a single emission line, and the star has a flat, featureless continuum. Then, $\sigma = \sqrt{N}$ for the unit-mean emission-line template and the S/N is *increased* over direct imaging by a factor \sqrt{N} . This is as expected intuitively, since we are simply excluding all flux from the star arising from wavelengths where the extrasolar planet does not emit, equivalent to centering a narrow filter on the emission line. The planet’s flux is preserved, but the star’s, and hence contaminating noise, is decreased. For 10^4 spectral data points, the S/N of the planet to star is $S/N = 100 \times s_p / \sqrt{S_0}$: we could see a planet a hundred times fainter by dispersing the light in this example, if we knew that its light arose from a single emission line. There may be practical application of this example at Ly α or other resonance scattered lines.

A single emission line maximizes the magnitude of the improvement, however there is obviously a middle ground between a δ -function and a completely featureless spectrum, where we may benefit from increasing the spectral resolution. Below, we examine plausible Jovian and terrestrial templates and find that for typical spectral windows this standard deviation implies a moderate *loss* of S/N compared to a direct image. There are however spectral windows where the parameter σ is large, and it increases as a function of the spectral resolution. Even so, the spectral approach can win in the next term, which is the elimination of systematic mis-subtraction of the host star.

3.1.3. PSF Matching Error

The third term in Equ. (2), $c_j = -S_0 \cdot \delta \cdot \sum_i T_i \hat{t}_{i-j}$, represents our ability to remove systematics and model or measure the reference PSF. This can be the limiting factor (Brown & Burrows 1990). Again, on the correlation peak, we have the error term

$$\begin{aligned} c_0 &= -S_0 \delta \sum_i T_i \hat{t}_i \\ c_0 &= -S_0 \delta \sum_i \hat{T}_i \hat{t}_i \end{aligned} \quad (6)$$

since $\sum_i \hat{t}_i = 0$ by definition, and $T_i = \hat{T}_i + 1/N$.

Typically, if the extrasolar planet spectrum is significantly structured in a way unrelated to that of the star, or if the velocity moves the spectrum more than the instrumental resolution, then the term $\sum_i \hat{T}_i \hat{t}_i$ is small. We can quantify the gain due to this systematic term as the ratio R of signal-to-error, Equations (3) and (6),

$$R = \frac{s_p}{S_0 \delta} \times \frac{\sum_i \hat{t}_i^2}{\sum_i \hat{T}_i \hat{t}_i}.$$

In the pure imaging case, this ratio (the planet’s signal to mis-subtracted stray light) is $R = s_p/(S_0 \delta)$, and hence using correlation techniques we gain by a factor $\sum_i \hat{t}_i^2 / \sum_i \hat{T}_i \hat{t}_i$. Equivalently, we reduce the host star flux by the inverse of this factor. This gain can be very large, from several tens to thousands. In § 3.2, we modify our procedure to (mathematically) make the gain infinite.

3.2. Gram-Schmidt Orthonormalization to Eliminate Stray Light

Again, the noiseless spectrum at a pixel is $S = S_0 T + s_p t$ which is a linear combination of the star and planet templates. The “basis vectors” T and t are independent but not necessarily orthogonal, and hence span a two dimensional vector space. The correlation functions we have been dealing with provide an inner product defined on that vector space

$$\langle d, t \rangle = \sum_i d_i t_i$$

and the norm of a function for this inner product is given by, say,

$$\| \langle x, x \rangle \| = \sqrt{\sum_i x_i^2}.$$

We can define a unit basis vector

$$\tilde{T} \equiv \frac{\hat{T}}{\|\hat{T}\|}$$

(i.e. such that $\langle \tilde{T}, \tilde{T} \rangle = 1$). Similarly, it will be convenient to define a scaled version of \hat{t} which has unit norm, $\tilde{t} = \hat{t} / \sqrt{\sum_i \hat{t}_i^2}$.

Given such a space, it is always possible to generate an orthonormal set of basis vectors that span the space, starting from any unit norm basis vector, such as \tilde{T} . (This procedure is known as Gram-Schmidt orthonormalization.) An orthonormal basis set is one whose

members *are* orthogonal, i.e. their inner product is zero, unlike the \tilde{t} and \tilde{T} vectors by themselves, and they have been scaled to have unit norm.

For a two dimensional space like ours, we can simply define the function

$$g = \frac{\tilde{t} - \langle \tilde{T}, \tilde{t} \rangle \tilde{T}}{\|\tilde{t} - \langle \tilde{T}, \tilde{t} \rangle \tilde{T}\|} \quad (7)$$

It is straightforward to show that $\langle g, \tilde{T} \rangle \equiv 0$, remembering that $\sum_i \tilde{T}_i^2 = 1$ by the definition of unit norm.

So what happens if we cross-correlate our spectra (i.e. derive the inner product) with the Gram-Schmidt function g that may be derived for any given planetary and stellar template pair? First, in the absence of noise, we derive our “signal” $\langle S, g \rangle \equiv \sum S_i g_i$:

$$\langle S, g \rangle = \langle S_0 T + s_p t, g \rangle$$

and $T = \hat{T} + 1/N$, $t = \hat{t} + 1/N$, $\tilde{t} = \hat{t}/\|\hat{t}\|$, $\tilde{T} = \hat{T}/\|\hat{T}\|$. Hence $S = S_0(1/N + \tilde{T}\sqrt{\sum_i \hat{T}_i^2}) + s_p(1/N + \tilde{t}\sqrt{\sum_i \hat{t}_i^2})$. Given that $\langle g, \text{constant} \rangle \equiv 0$ since we are dealing with the zero mean versions of the templates, and that $\langle \tilde{T}, g \rangle = 0$ by the construction of g , it follows that the signal

$$\langle S, g \rangle = s_p \sqrt{\sum_i \hat{t}_i^2} \langle \tilde{t}, g \rangle \quad (8)$$

or in other words the terms involving S_0 , the stellar component, and any constant offsets *drop out*. This is the same as the signal obtained from cross-correlation, but for zero stray light error, noting the different scalings used for the templates and modified by the inner product of \tilde{t} and g .

The term $\langle \tilde{t}, g \rangle$ measures how orthogonal the planetary template is to the stellar template. We can expand this inner product to find that

$$\langle \tilde{t}, g \rangle = (1 - \langle \tilde{T}, \tilde{t} \rangle^2)^{1/2}$$

where, as in the cross-correlation section, the quantity $\langle \tilde{T}, \tilde{t} \rangle$ is typically very small.

We may, as above, derive a variance for the inner product of S with g assuming only Poisson photon noise. Similar to before, if $w = \sum_i g_i \epsilon_i$ then $E(w^2) = \sum_i g_i^2 \sigma_i^2 = S_0 \sum_i g_i^2 T_i$. Hence $\sigma^2(w) = S_0 \sum_i \hat{T}_i g_i^2 + S_0/N \sum_i g_i^2$, however g has unit norm, $\sum_i g_i^2 = 1$ so

$$\sigma^2(w) = \frac{S_0}{N} + S_0 \sqrt{\sum_i \hat{T}_i^2} \sum_i \tilde{T}_i g_i^2 \quad (9)$$

which is similar to the cross-correlation version, Equ. (4).

We can therefore write a S/N for the Gram-Schmidt orthonormalization by combining Eqs. (8) and (9).

$$S/N = \frac{s_p}{\sqrt{S_0}} \times \sigma(t') \times \langle \tilde{t}, g \rangle / \sqrt{1+h} \quad (10)$$

where again we have made use of the identity $\sigma(t') = \sqrt{N \sum_i \hat{t}_i^2}$ and $h = N.S_0 \sqrt{\sum_i \tilde{T}^2} \langle \tilde{T}, g^2 \rangle$. We expect h to be small, and as above, $\langle \tilde{t}, g \rangle \approx 1$, so the loss in S/N that might have been anticipated by moving to a truly orthogonal basis is very small indeed. *The S/N of the Gram-Schmidt method is essentially the same as that of the cross-correlation technique, but with the advantage that stray light is completely eliminated.*

Note also that, in principle, with the Gram-Schmidt approach we do not need to carry out additional PSF estimation and subtraction. In practice that may still be desired, but under these idealized conditions it is not needed. Finally we note that this method will only operate effectively where the planet spectrum differs significantly from that of the star, either because of atmospheric spectral features or velocity shifts. The spectral templates we constructed, below, are the as-observed Jovian spectrum and a terrestrial template, and they do display substantial structure which distinguishes them from the star. Woolf et al. (2002) present the integrated spectrum of the Earth derived from Earthshine observations, and they show empirically that strong atmospheric absorption features are indeed prominent.

3.3. Analysis of Variance

Cross-correlation with a matched template offers a good strategy for finding a signal in a noisy dataset. If, however, we do not have a template, progress can still be made provided that there are spectral differences between the star and extrasolar planet. The noiseless spectrum at a pixel is $S = S_0T + s_p t$, a linear combination of the star and planet templates multiplied by a flux contribution from each. The “basis vectors” T and t are independent but not necessarily orthogonal, and hence, as discussed in § 3.2, span a two dimensional vector space. A variety of methods exist to determine the dimensionality of a distribution of points in such a space. Principal component analysis may be used to determine how many basis vectors are needed to describe the distribution. Closely related to this, and sufficient for our purposes is a simple analysis of variance.

We may, in principle, derive a very high S/N mean stellar spectrum template empirically from the integral-field observation itself, estimate the flux at each position from the observed value and then subtract a scaled mean. Analysis of the variance of the residuals can offer a

statistical statement about the likelihood that the photon distribution arises only from the stellar host spectrum. The variance of the residual distribution for a given pixel follows the χ^2 distribution, and so it is easy to quantify the probability that the observed distribution could have arisen under the null hypothesis: that there is no planet present.

A generalized statistical approach such as the analysis of variance is attractive because it requires no knowledge of the character of the planetary template. Clearly, having established that significant excess variance exists (or an equivalent statistical statement), one would then interrogate the spectrum in more detail to either derive an empirical flux distribution, or else to quantify its similarity to a variety of predetermined templates and hence deduce its nature. In our simulations below, we illustrate application of a χ^2 statistic.

4. Simulations for Spatially Invariant Spectra

Obviously these are idealized approaches in terms of the concept of the datacube, and the statistical techniques are straightforward. However, they serve to emphasise the principle that there are mathematical and statistical approaches to data analysis, in addition to specialized hardware, which may contribute significantly to solving problems in extrasolar planet detection and characterization. In § 4 we proceed to illustrate application of the formulae of § 3. Given the assumption of a spatially invariant spectrum (after filtering out low order differences), this may be considered as an idealized representation of a time-averaged ground-based observation, or of a space based observation over either a limited wavelength range or close to the host star where diffraction effects do not cause high frequency ripples.

4.1. Derivation of Template Spectra and the Photon Budget

We will consider Solar illumination of Jupiter and the Earth as the basis for our templates. One of the fundamental parameters whose influence we wish to study is spectral resolution. We therefore attempted to obtain template spectra at the highest possible spectral dispersion, which may be degraded to lower spectral resolution, or not, depending on the application.

Simulation of very high resolution spectra reflected from planetary surfaces, particularly terrestrial ones, is complicated by the fact that the atomic and molecular features of most interest are the very ones that hamper astronomical observation of astronomical targets. Rather than strive for ultimate accuracy therefore, we have created a set of illustrative, but realistic, templates as described in the following section. All spectra were resampled

onto a uniform grid in $\log\lambda$ with a constant resolution $\lambda/d\lambda = 500,000$ using standard interpolation routines. Shifting and cross-correlation of a template onto a logarithmically sampled spectrum corresponds to a velocity shift.

(i) *A Solar template* was generated from the Solar model of Kurucz derived using the program “ASUN” and available from Kurucz’s website <http://cfaku5.harvard.edu/>. The file used was *irrcmasun.asc* in the [SUN.IRRADIANCE] directory. We further processed this model to normalize by the local continuum (presented in the file) and resampled onto a uniform grid in $\log\lambda$ with a constant resolution $\lambda/d\lambda = 500,000$. This was done using spline interpolation. We decided to use a model atmosphere in order to avoid problems in the regions of most interest: namely where there is a large amount of molecular structure arising from terrestrial absorption. While in detail the model atmosphere may differ from the actual Solar spectrum, it is quite adequate for our purposes in providing a statistically realistic distribution of lines, line densities and depths. The resulting continuum normalized template Solar spectrum is shown in Fig. 1.

(ii) *A Jovian template* was made, which is a hybrid high-resolution Solar spectrum (the one described above) multiplied by a moderate resolution spectrum of the Jovian albedo from Karkoschka (1994). Karkoschka (1994) and (1998) presents and discusses the albedo of Jupiter and the other outer planets from 3000 \AA to $1.050 \mu m$. The resolution is $\approx 10 \text{ \AA}$, or $R \sim 500 - 1000$. We kept the reflected Solar component at the full resolution above. In reality, there may well be additional fine structure apparent at high resolution in the Jovian albedo. For example, Tokunaga et al. (1979) show numerous emission lines in the $10 \mu m$ window for Jupiter, emission from C_2H_6 , and reviewed by Larson (1980). Rotational broadening may enter at our full resolution since $R = 500,000$ corresponds to velocity $v = 0.6 \text{ km.s}^{-1}$, or 1.2 km.s^{-1} for two pixel width bin. The equatorial speed of Jupiter is 12.6 km.s^{-1} , however the majority of the reflected light arises from the disk center regions where the relative velocity is much closer to zero, and additionally any inclination of the planetary pole out of the sky-plane further reduces rotational broadening. We did not make any correction for rotational broadening in our analysis. The resulting spectrum is shown in Fig. 2 as a function of resolution.

(iii) *A Terrestrial template* was generated with absorption features only. Again, for an incident spectrum, we used the Kurucz model above. To estimate the atmospheric absorption spectrum, we used the three atlases of the Solar spectrum Livingston & Wallace (1991), Wallace, Hinkle & Livingston (1993), Wallace, Hinkle & Livingston (1998) which present Fourier Transform Spectra of the Sun from 3570 \AA to $5.4 \mu m$ at a resolution of order 200,000 to 400,000 over the majority of the wavelength range ($\lambda > 5000 \text{ \AA}$). These atlases present atmospheric transmission functions at high spectral resolution which are well-suited for our

purpose. To generate a terrestrial template, we multiplied the Kurucz model by the square of the atmospheric transmission (squared to allow for the fact that light reflected from the surface of the Earth has to pass through the atmosphere twice). Fig. 3 shows the resulting terrestrial template spectrum. In this case, as spectral resolution grows, the complexity of the absorption features continues to grow. The dominant bands are from oxygen and water, and may also be seen in the observed spectrum of Woolf et al. (2002). Fig. 4 expands the region around the prominent molecular oxygen A-band and offers a sense of the level of complexity that arises as spectral resolution increases.

(iv) *Another Terrestrial template* was generated with absorption and a selected set of emission lines from the Meinel series of OH lines in the near-IR. We were interested in understanding whether atmospheric emission lines might be detectable from extrasolar planets. This could only occur because they are extremely narrow, which allows, in principle, rejection of the continuum starlight in a fashion analogous to, but the reverse of, a terrestrial OH-suppression device.

By far the brightest line emission from the night-time airglow is from the Meinel series of OH radical vibration-rotation complex (Meinel 1950, Krassovsky, Shefov & Yarin 1962, Leinert et al 1998). The intensities are highly variable and decrease through the night (Ramsey et al. 1992). A typical total intensity is of order 5 MR (Leinert et al 1998). We obtained a list of bright OH lines (only) in the $1\mu m - 2\mu m$ range in order to understand their likely relevance. This was downloaded from the Cambridge OH Suppression Instrument (COHSI) web page, <http://www.ast.cam.ac.uk/~optics/cohsi/www/ohsky/database.htm>, which draws from Maihara et al. (1993) and Olivia & Origlia (1992). To estimate an order of magnitude amplitude at which to insert these lines, we first converted the tabulated intensities to Rayleighs and then estimated an approximate terrestrial reflected Solar spectrum. The (low resolution) flux spectrum of the Sun obtainable from the Hubble Space Telescope (HST) calibration library *crcalspec* within *iraf/stsdas* was used, with a Bond albedo of 0.306 for the Earth. The solid angle of Earth from the Sun is 5.7×10^{-9} sr, and the total scattered flux is 1.4×10^{-10} that of the Sun, hence the approximate surface brightness of the Earth in $R \text{ \AA}^{-1}$ is $R_E \approx 3.06 \times 10^{-7} S_\odot$ where S_\odot is the Solar flux expressed in photons $s^{-1} \text{cm}^{-2} \text{\AA}^{-1}$. Given the large variability of these lines, and to better assess the difference they make, we arbitrarily increased their intensities from the tabulated value by a factor 5, corresponding to a total intensity of 3.2 MR in these lines.

Fig. 5 shows the resulting spectrum, again normalized to the continuum level. As can be seen, the OH lines do start to become evident for very high spectral resolutions, although their strength never rises to dominate the spectra. Additional work on atmospheric line emission further into the infrared, or possibly ultraviolet, may prove interesting. In the IR,

some of the strongest emission lines occur where water vapour strongly absorbs incident sunlight, and so the relative contrast between the emission and absorption spectra may be very different. Also, the character of the night and day emission spectra differs substantially (Zipf 1966, Le Texier et al 1989).

4.2. Quantitative Characterization of the templates

In order to design an experiment, Equ. (5), which gives the S/N of the cross-correlation peak, may be used for a given template to plot σ , $s/\sqrt{S_0}$, and hence S/N as a function of wavelength, for a chosen spectral interval or resolution. In other words, the correlation function contains more information in regions where the spectrum is highly structured and these plots allow such spectral windows to be identified. Figs. 6 & 7 show the case of 2% sampling intervals for calculating these parameters. It suggests that we either go to the blue, where there are strong photospheric absorption features from the illuminating star (in our case, the Sun), or else to the near infrared where strong molecular absorption features in the planet’s atmosphere dominate. Since the latter differentiate the extrasolar planet from the star, this is the region we choose to study.

For the purposes of analysis and simulation, we selected a spectral region that seems to be a plausible candidate for studies of the type we advocate. This primary region is essentially the I -band, from 7000Å to 1 micron, where strong water and oxygen absorption features are present in the terrestrial spectrum, and deep, broad methane absorption features are apparent in the Jovian spectrum. In future work it may be of interest to select, for example, a very narrow window around the oxygen A-band from 7580Å to 7800Å, in order to attempt specific targetting of terrestrial extrasolar planets with oxygen in their atmospheres, provided the photon budget permits it.

The other parameters of the spectral templates which offer an indication of the utility of the correlation function are the width and contrast of the autocorrelation function, and the variance (i.e. degree of spectral structure) as a function of spectral resolution. The autocorrelation functions are shown in Figs. 8 and 9, showing the very narrow peak in the terrestrial version, indicative of the wealth of structure present at high spectral resolution.

Figs. 10, 11 and 12 show the run of standard deviation of the unit-mean template with spectral resolution for each example. For the terrestrial template, Fig. 10, we see a σ that increases continuously, to the limit of our resolution. The value of σ is in the range 0.1 — 0.2, corresponding to a S/N about 20% that obtained by direct imaging alone. (Recall: we still have the direct image; the spectral dimension is adding extra information.) The

A-band region shows similar behaviour, though with an overall dispersion that is larger, corresponding to about 40% of the imaging S/N . The Jovian template has a high degree of structure even at relatively low spectral resolution, and it saturates at resolutions of a few hundred. This may be an artifact of the hybrid nature of the template, or else it may be that the broad methane bands do not contain additional fine structure. If there is additional fine structure, then the dispersion can only increase and hence the S/N too.

Finally, we consider the “gain” term which is the reduction of stray light by the cross-correlation process. The gain term R is

$$R = \frac{s_p}{S_0 \delta} \times \frac{\sum_i \hat{t}_i^2}{\sum_i T_i \hat{t}_i}.$$

and is dominated by the function $\sum_i \hat{T}_i \hat{t}_i$. For the spectral regions we selected, there is little correlation between the stellar and planetary templates. There is no physical constraint on whether the quantity should be positive or negative, and indeed as we shift the relative velocities, the function can, and does, pass through zero, corresponding to infinite gain and complete rejection of the stray stellar light (albeit not the noise from that light). These functions depend in a sensitive way on the template, the spectral region, the relative velocity and the spectral resolution, so rather than attempt to span this large and somewhat unstable parameter space, we hark back to § 3.2 and note that infinite gain may be forced mathematically. Suffice it to say that gain values ranged from several tens to thousands for the examples we studied.

Thus, if the dominant error term is the subtraction of the PSF, then we could gain over direct imaging according to the product of the dispersion of the template (which typically reduces S/N somewhat) and the gain function, which greatly decreases the contaminating starlight.

4.3. Photon Budget

Aside from all other considerations, it is clearly necessary that there be sufficient photons from the extrasolar planet we seek so that detection is at least possible. The smallest aperture that might be considered for direct planet imaging is ~ 2 -m, similar to the aperture of HST. Space telescopes of order two to ten meters diameter are under consideration for extrasolar planet finding and characterization, while ground based concepts can reach many tens of metres diameter. For an order of magnitude estimate, we assume an Earth/Sun flux ratio of 1.04×10^{-10} and a Jupiter/Sun flux ratio of 5.18×10^{-10} . Scaling from the number of photons that would be detected by the Advanced Camera for Surveys on HST in the F814W filter

(the I -band), which is $2.6 \times 10^{10} \text{ sec}^{-1}$ for the Sun at 1 pc, we derive Table 1 which gives the number of photons for various apertures and distances. We also consider two bandpasses: the I -band and a small window centered around the molecular oxygen A-band, a possible biomarker spectral feature. If typical background Poisson noise levels can be brought down to of order a few hundred or a thousand counts, there are adequate numbers of photons from the extrasolar planets in many circumstances that direct detection may indeed be contemplated.

4.4. Simulation for the Cross-Correlation Approach

Cross-correlation methods would be applicable for configurations that result in a uniform spectrum across the field of view, such as most ground based approaches, but also space based either over limited wavelength ranges, using averaging or using specialized filtering methods. For an example configuration, we used a simulated coronagraphic observation kindly provided by John Krist (STScI), which is typical of those expected from the recently installed Advanced Camera for Surveys on HST, using its aberrated beam coronagraph. The filter used for the simulation was the F435W filter, although since *we are only interested in showing the numerical approach* this is unimportant. The surface brightness profile of this aberrated beam PSF is similar to estimates of the ideal performance of ground-based adaptive optics coronagraphs in the infrared (e.g. Itoh et al. 1998, Beuzit, Mouillet & Le Mignant 2000). We simply need a PSF that demonstrates some of the generic complexities that might be encountered, either in space or on the ground hence we adopt this PSF for our calculations. Fig. 13 shows the coronagraphic image.

A second simulation was also provided with typical parameter variations seen in HST: slight “breathing” differences and slight mis-centering of the star on the two frames. This second simulation offers us a benchmark, as it allows us to compare the idealized mathematical results with what is one of the most powerful actual techniques currently in use on HST, namely “roll deconvolution”. In this approach, a second PSF of a star is obtained with the telescope “rolled” around the axis pointing towards the star. The PSF remains unchanged, while the image of the extrasolar planet is moved from its original location. Differencing of the two PSFs results in the roll-deconvolved image. (This is one way of estimating PSFs, parameterized by δ in § 3.1.) This second simulation offers a plausible amount of mis-match between the two PSFs one might obtain in practice.

We are not attempting to provide the limits to which the techniques may be pushed, so we adopt the most optimistic scenario plausible, following Brown & Burrows (1990), which is of Jupiter orbiting a (strictly) Solar type star at 1 pc, at a radius of 5 a.u., i.e. like Alpha Cen A and B. An reasonable upper limit to the integration time is $\sim 10^5 \text{sec}$, or $\sim 30 \text{ hr}$,

beyond which terrestrial planet orbital motions would begin to smear their images, so this is the fiducial integration time we adopt. Since the simulation is for a 2-m telescope, the equivalent 8-m observation would correspond to a distance of ~ 4 pc (although hopefully such a telescope would not require an aberrated beam coronagraph!).

There are a number of free parameters, not least of which is the data volume consideration. We used a 150×150 pixel quadrant of the PSF, sampled 0.025 arcsec per pixel spatially, and a spectral resolution of 800 sampled twice per resolution element to provide spectra from 7000\AA to $1\ \mu\text{m}$. This results in a datacube of dimensions $150 \times 150 \times 571$.

In generating the spectral dimension we assumed the PSF remained the same over the spectral window, that the stellar spectrum was as given by the Kurucz model template, above, and we added planets with their templates spectra, as described above. We added Jupiter at 5 a.u., and, to test the numerical methods, “bright Earths” at 1.5, 2 and 3 a.u. with flux ten times that of the real Earth. The flux ratio assumed for the Jovian planet was 5.2×10^{-10} of the star and the bright-Earths 1.0×10^{-9} . At the location of the Jovian planet, the PSF wing level is 1.6×10^6 photons per pixel, about $9\times$ the peak in the planet. The expected ideal imaging $S/N \sim 145$ from Poisson statistics, although the empirical noise level is some $300\times$ the photon noise due to PSF fine structure, and the planet is not visible. For the bright Earths, the PSF wing levels are 4.1×10^8 , 1.6×10^8 and 2.0×10^7 with planet peak flux $\sim 370,000$ counts.

Firstly, to show the best that might currently be attainable in practice, Fig. 14, we simulated a realistic “roll deconvolution” by differencing the two coronagraphic simulations from one another. Slight miscenterings and focus changes (breathing) were introduced between the two. The Jovian extrasolar planet is visible in the top right corner of the roll-deconvolved image. The fine-structure noise is reduced by a factor ~ 10 and the planet is visible with an $S/N \sim 6$.

We now turn to the mathematical methods of § 3. Fig. 15 shows an image of the cross-correlation function c_0 from Equ. (2) for the roll-deconvolved datacube using the hybrid Jovian template;

$$c_0 \equiv \sum_i d_i \hat{t}_i = \sum_i \epsilon_i \hat{t}_i + s_p \cdot \sum_i t_i \hat{t}_i - S_0 \cdot \delta \cdot \sum_i T_i \hat{t}_i$$

This time the Jovian planet is very clearly visible in the top right corner. The S/N of the simulation is close to the theoretical values given above. We expect the photon S/N to be reduced by a factor $\sigma_J = 0.39$ from the structure level in the Jovian template, to about 50–60. The gain factor G for the Jovian template in this simulation is large, at $G = 1347$, hence we expect photon statistics to dominate. In fact in the cross-correlation image, the

peak planet flux to local (empirical) noise gives $S/N \approx 43$ in good agreement with the theory (and much better than the $S/N = 6$ of the roll-deconvolution).

The cross-correlation with the terrestrial template, Fig. 16, also reveals the bright Earth, but the Jovian planet does not appear (it is actually a slight depression). This indicates that a good template match is important. Sensitivity to the template match is a two-edged sword: on the one hand, detection in the general case is made more tricky, but on the other hand, it reveals potentially important information about the spectrum of the extrasolar planet. The gain factor for the terrestrial template is lower, at ≈ 80 consistent with the higher degree of residual structure seen in this image.

Fig. 17 shows the analysis of variance image, an image of reduced- χ^2 with a strong peak at the location of the Jovian planet, and a second faint one at the position of the outer “bright Earth”. The probability associated with the reduced- χ^2 thresholded at $5\text{-}\sigma$ is shown in Fig. 18 and indeed there is a statistical signature of both planets present.

Next, we produced images of the Gram-Schmidt correlation function image using the Jovian template, Fig. 19, applied to the *single original* (not roll-deconvolved) coronagraphic datacube. The Jovian planet is clearly visible, and the remainder of the image shows only noise expected from photon statistics, with numbers essentially as for the cross-correlation ($S/N = 43$). Fig. 20 shows the Gram-Schmidt correlation function image using the terrestrial template also applied to the original coronagraphic datacube. The outer bright-Earth planet is clearly visible, and there are hints of the inner two. If we lightly smooth this image, all three are easily seen, Fig. 21. The remainder of the image shows only noise expected from photon statistics. The Jovian planet does not appear, demonstrating the importance of template matching.

As we progress through this sequence, the ability to detect extrasolar planets within the wings of the stellar PSF increases dramatically. This is because huge gains can be made in reducing the systematic residual term, to the Gram-Schmidt orthonormalization limit where it is eliminated completely. The S/N of the correlation peak is related simply to the S/N of the ideal image, multiplied by the standard deviation of the planet’s template normalized to unit mean. If there is a large dispersion in that template, i.e. the planet has lots of spectral structure, then we can in principle gain over direct imaging alone. In practice, for the templates studied here, that standard deviation was in the range $\sim 0.15 - 0.8$. Despite a loss of a factor of several in S/N compared to the ideal imager, the dramatic gains in the systematic term clearly result in a better detection capability. If these techniques are to be applied in practice, we must also understand the degree to which the assumption of spatially similar spectra can be realised, a study which has many free parameters and which is beyond the scope of this work.

5. Diffraction Dominated PSF: Spectral Deconvolution

5.1. Concept and Illustration

While the previous section explored the concept of pattern recognition where the spectra of each pixel were identical, we now look at the effects of potentially strong amplitude modulation of spectra introduced by wavelength dependencies in the PSF. A monochromatic diffraction limited coronagraphic PSF with a plausible suite of aberrations, contains a spectacular degree of structure. This may broadly be characterized as a set of rings, the Airy pattern due to diffraction by the telescope optics, with spacing at the diffraction limit of the telescope λ/D (where D is to be corrected by the Lyot stop) together with a multitude of speckles due to scattering from mid-frequency surface irregularities also of typical dimensions λ/D . As wavelength increases, the ring pattern scales to larger size proportional to the wavelength, and the speckles also grow larger proportional to wavelength. At an angular radius x , therefore, we expect a characteristic change of the spatial PSF (with wavelength) to produce a modulation (i.e. variation in apparent flux as Airy rings and speckles move across the pixel) in the spectral dimension at a characteristic scale of $d \ln \lambda \equiv d\lambda/\lambda \sim (\lambda/D)/x$ where x is in radians, i.e. (spatial resolution)/(angular separation). For $\lambda \approx 1 \mu\text{m}$ and $x \sim 5 \text{ arcsec}$, $d\lambda \sim 200 \text{ \AA}$. In other words we expect modulation on a characteristic spectral scale of $d\lambda/\lambda \sim 0.02$.

It is possible to remove some of this spectral modulation using a variety of techniques. Ftaclas et al (1994), for example, advocate use of very broad bandwidth imaging to suppress the fine structure. Fourier filtering could be used (since there is a very characteristic set of spectral frequencies involved), however in the example used above, the spectral frequencies of the hybrid Jovian template are quite similar to those of the diffraction modulation, and so Fourier filtering runs the risk of eliminating much of the signal from the planet.

Instead, making a virtue of necessity, we offer a simple and rather effective method to eliminate the stellar PSF in this case, which we call “spectral deconvolution”. To illustrate, we again used the code of John Krist to generate a set of monochromatic PSFs from 7000 \AA to $1 \mu\text{m}$ for a 2.0-m telescope with a Lyot-coronagraph reducing the pupil diameter by 20%. A Gaussian occulting spot with $\text{HWHM} = 0.3 \text{ arcsec}$ was used. A mid-frequency rms surface error of 0.5 nm was assumed, significantly improved over that of HST. A suppression factor for the host star of 0.6×10^{-3} results. The PSF was sampled with 0.025 arcsec pixels and a field of view 300×300 pixels (10.6 arcsec corner to corner) and again a spectral resolution of 800 corresponding to 571 spectral slices uniformly spaced in $\log \lambda$. To add planets we generated a simulated self-consistent PSF for a point source not lying beneath the coronagraphic hole. We again used Jupiter at 5 a.u. and extra planets at 1.5, 2 and 3 a.u. with ten times Earth

flux. The flux ratio of the Jovian planet and bright Earth’s to the host star was 5.6×10^{-10} and 1.0×10^{-9} respectively. This time we did not impose spectral structure on either the star or planets, but simply adopted the same total counts in each spectral slice. In principal spectral realism could be included, however the simplicity of the concept proposed is quite well-shown without this additional complication.

The extrasolar planetary system was placed at a distance of 2 pc, and fluxes were normalized to those of a Solar type star at that distance for a 2-m telescope and 10^5 sec integration time. Poisson noise was added to each image.

Fig. 22 shows the average PSF of the datacube, with the extrasolar planets. Clearly the planets are completely hidden in the scattering wings of the stellar PSF. Following Brown & Burrows (1990), the structure is dominated by PSF fine structure. The empirically measured noise at the location of the Jovian planet is $\approx 75\times$ the photon shot noise. The amplitude of the stray light in the wings of the stellar PSF is $\approx 8.9 \times 10^5$ photons per pixel compared to a peak flux in the Jovian planet of 11,800 photons per pixel. That is, the planet’s peak flux is only 1.3% that of the local stray light. In the notation of Brown & Burrows (1990), $Q = 0.013$. If we were photon noise dominated, the $S/N \approx 12.5$ for such an observation, however the PSF fine structure results in $S/N \sim 0.2$ and the extrasolar planet is undetectable.

The four left hand panels of Fig. 23 show slices through the datacube prior to the light smoothing that was applied, at four separate wavelengths from 7000\AA to $1\mu\text{m}$ (bottom to top). Inspection of these figures shows the expected expansion of the PSF with wavelength as features move out and everything scales with wavelength. Fig. 24 picks a pixel at the radius of the Jovian planet, and shows the spectrum along the datacube at that pixel. The modulation at this resolution is very large due to these diffraction effects as structures move across the pixel.

Now we adjust the spatial scale of the datacube as we progress through it in wavelength. An image at 9000\AA , say, is shrunk by a factor $9/7$ to match the PSF at 7000\AA and a new datacube is constructed. The four right hand panels of Fig. 23 in contrast to the previous datacube show that there is far less difference between the PSFs as a function of wavelength when resampled spatially. A plot along the spectral dimension at the same pixel as before, Fig. 25, now shows only a smooth, slowly varying component that can easily be modelled with a polynomial fit. The procedure is to make such a fit, subtract it from the datacube, and then resample the data back onto the original spatial scales.

If there is additionally a smooth scattering component as well as the diffraction dominated speckles and rings, that too would enter as a low spatial frequency component and

would not make any difference to the effectiveness of the method.

In the spatially resampled datacube, apart from the first few slices, *the planet has been moved away from its original pixel*. It now occupies a straight diagonal slice through the datacube starting at its original location (radius r_0) and ending at a radius $r_1 = (\lambda_0/\lambda_1)r_0$ along the radius vector to the planet from the star. The fractional width along the spectrum is $d\ln\lambda/\Delta\ln\lambda \sim dx/(r_0\ln(\lambda_1/\lambda_0))$ where $\Delta\ln\lambda$ is the logarithmic width of the entire spectral window, and dx is the diffraction width of the planet’s PSF. Note that the shrinking of images with increasing wavelength preserves this width. *Hence, when a low order polynomial is fitted to the spectrum at a particular pixel, the flux from the extrasolar planet is largely ignored, as it represents a high order term that the polynomial cannot reproduce.*

Having subtracted the emission from the star, we can now reconstitute the original (but subtracted) datacube by resampling the subtracted data back onto its original spatial scale. When the datacube is resampled back to its original dimensions and scale, this residual planet flux realigns itself once more, and the elements of its flux line up spatially. Collapsing the datacube along the spectral dimension makes the extrasolar planet become visible.

In addition, while the host star spectrum at the location of the extrasolar planet is very strongly affected by diffraction, *the spectrum of the extrasolar planet is unaffected*. The planet location is obviously the center of its Airy pattern and hence, apart from a slow change in peak brightness as resolution decreases to longer wavelength, the spectrum of the extrasolar planet is fully preserved.

Fig. 26 shows exactly such an image from the simulation described. Light spatial smoothing was first applied to avoid sampling problems (a 2-D Gaussian $\sigma = 1$). The NOAO iraf utility *imlintran* was used with ‘sinc’ interpolation to resample the images, both to compress and re-expand, and a fourth degree polynomial fit and subtraction was carried out for each “spectrum”. The final subtracted, reconstructed datacube was collapsed along the spectral dimension to produce the image shown in Fig. 26.

The Jovian planet is easily visible, as is the outer one of the additional planets we added. Interior to this (3 a.u. at 2 pc), residuals from the star again dominate, and the effectiveness of the method diminishes as the ratio dx/r_0 increases and the planetary signal becomes lower (Fourier) frequency in the spectral dimension. Quantitatively, the peak in the Jovian planet’s signal is ≈ 6000 photons per pixel and the empirically measured noise around it is ≈ 290 photons per pixel. Given that we spatially smoothed a noise field which originally had $\sigma = 950$ photons per pixel we expect the Poisson noise to reduce to $\sigma \approx 220$ photons per pixel, consistent with our measurement. This smoothing also accounts partially for the slightly lower peak planetary flux. In other words, the detection achieved is $S/N \approx 20$,

compared to a Poisson limit in the range 12–40 depending on the level of spatial smoothing employed. Recall that the peak flux of the extrasolar planet is only 1% of the level of the PSF wings.

In this simulation $S_0 \sim 9 \times 10^5$, $N \sim 600$ so the requirement that the noise not be dominated by detector readnoise is $\sigma_R < 38/\sqrt{n_{exp}}$. For a readnoise of, say, 4 photons, we could take 100 exposures and satisfy this constraint. Alternatively we may reduce the spectral resolution and shorten the exposure time of individual exposures, provided we keep the extrasolar planet signal in only a small fraction of the spectrum in the resampled datacube.

Fig. 27 illustrates the idea further by showing cuts through the datacubes along one spatial and one spectral dimension, for both the original cube and the spatially resampled cube. The diverging diffraction pattern changes to a series of smoothly changing “spectra” that can be modelled and subtracted, leaving the planet spectrum as a diagonal in that datacube. Improved tuning of the reconstructed image may be obtained by allowing for the varying noise as the stray light amplitude varies with wavelength, with $1/\sigma^2$ weighting being optimal.

This simulation was carried out in a very simple and straightforward fashion. It ought to be possible to reach the ideal Poisson imaging limit with this method. The factor that would limit the derived S/N is the level to which a spectrum can be modelled and subtracted with low frequency components. If there were high spectral frequency features *arising from the diffraction and scattering* (not intrinsic to the source), they would enter into the noise of the final image. The expected frequencies are low, however, and no high frequency features were found in the simulation we ran. In practice of course the star has a somewhat complex spectrum, however it is a well-known spectrum and it should be possible to adjust its low-order shape to achieve a good match to the observations. Ultimately, it may even be possible to combine a matched filtering or orthonormalization approach with spectral deconvolution method (e.g. by testing whether a specific pixel hosts an extrasolar planet using corresponding matched filters in the appropriate adjacent pixels of the spatially resampled datacube).

If we scale the simulation to an optical coronagraphic 8-m TPF concept, with mid-frequency surface errors unchanged (0.5 nm), then the radial distance of the planet would be now 1.2 a.u. and the background and planet would have $\sim 16\times$ the flux. Consequently, to detect a terrestrial luminosity planet five times fainter than Jupiter to $5\text{-}\sigma$ we would require $\sim 25,000$ sec or 7 hrs. If we allow spatial smoothing to improve S/N, as before, the required exposure time is only $\sim 10^4$ sec. Equivalently, Jovian planet detection for a 2-m telescope requires only $\sim 6,000$ sec, scaling the $20\text{-}\sigma$ result in 10^5 sec back to $5\text{-}\sigma$.

There are a number of very appealing aspects to this method. Firstly, we can essentially achieve the theoretical Poisson limit for direct imaging, irrespective of the spectral character of the extrasolar planet. By contrast the S/N achievable in the cross-correlation and Gram-Schmidt method depends on the variance of the planet’s spectrum. Standard coronagraphic techniques are typically limited to *much* higher flux levels due to the mid-frequency errors. Secondly, and obviously, having located the extrasolar planets using a spectrum, we have at our disposal a spectrum of the extrasolar planet from the outset and so we can in a very general way immediately begin to study its character. Thirdly, we only require a single observation to detect the candidate planet, hence we need PSF stability only over the duration of the observation. Since we design the experiment to be Poisson limited, the shortest possible integration times could be used and processed independently. This may alleviate PSF stability issues that are of concern under some circumstances.

5.2. Related Observations and Applications

A variation on the theme of this method is to obtain multiple images using narrow-band filters sequentially, and then pursue similar resampling and subtraction (spectral deconvolution) with a datacube built from the sequential filter observations. The wavelength sampling interval needs to satisfy two constraints (i) the planet should move by a significant distance when the image scale is adjusted in proportion to wavelength (ii) there needs to be enough data points in the pseudo-spectrum that the planets spectrum occupies only a small element within it. (An equivalent strategy is to build a datacube using a long-slit spectrograph with adjacent spectra taken sequentially, as in Fig. 27.)

Recall from the above discussion, that to move a full diffraction width of $dx = \lambda/D$, we would require $\Delta\lambda = \lambda \times dx/x$. This approach offers a straightforward route to experimental design. For example, if $dx = 0.05$ arcsec and $x = 2$ arcsec, at 5000\AA we would need to change wavelength by 125\AA , which is well-suited for example to the parameters of the narrow-band ACS ramp filters. Clearly it would be highly desirable to obtain more realistic simulations, together with some exploratory observations to determine how well this works in practice in the presence of slowly changing optics.

In principle there are three major advantages and one disadvantage compared to roll-deconvolution. (i) The telescope does not need to be moved. We eliminate aberrations due to mis-centerings between successive observations that plague roll-deconvolutions. (ii) We are insensitive to low frequency modulation which telescope “breathing” would typically cause, and we can reduce this further by keeping exposures short. (iii) We are always on-target so the planet flux continues to integrate. There is no dead time while reference PSFs are

obtained. On the other hand, the disadvantage is that we no longer “spectrally multiplex” and so additional exposure time is needed to accumulate the same number of photons. If we are only interested in detection, rather than characterization, then we would need to consider observations in the blue where spatial resolution is improved, versus the red where the speckle pattern becomes less severe.

The spectral deconvolution technique, if it lives up to its promise, has the potential to be applied to a high fraction of space-based coronagraphic observations, beyond planet searches. These may include probes of dust disks around stars and the host galaxies of QSOs. The case of QSOs may be particularly interesting as the combination of strong emission lines in the QSO and possibly its surroundings will provide a challenge to data analysis, and raises the possibility of trying to combine correlation and spatial scaling techniques.

This method depends on the datacube possessing mostly diffraction behavior (a smooth scattering component would not reduce its efficacy), and hence is most appropriate for space-based concepts. If the bandwidth is small (as might be the case for focussing on specific spectral features) or if the PSF structure is color-insensitive (e.g. as caused by the atmosphere) then the cross-correlation approaches above are likely to prove more effective.

5.3. Practicalities

Application of any of these ideas to real optical systems will require careful consideration of numerous practical difficulties. Not least of these is construction of an integral field spectrograph of the dimensions envisaged, especially in the first part of the paper. Inefficiencies in the optical system inevitably arise in a real spectrograph, and difficulties may arise from scattered light internal to the spectrograph and interference fringing within the layers of the detector itself. Many CCDs are especially prone to moderate or large amplitude fringing in the very red regions in which we are most interested.

Data volume, too, is likely to be an issue. Ideally one would like a large spatial coverage, high spatial resolution, and moderately high spectral resolution. The reason this problem does not need to become completely uncontrolled is that we seek planets close to their host stars, and hence the spatial coverage may be restricted to the region of interest.

Finally, if compromises must be made such as abandoning spectral multiplexing, then the degree of achievable stability enters the trade space as we design our observations.

Despite these and other difficulties that may be encountered in practice, it will be worthwhile to obtain a set of test observations and gain actual experience of dealing with

the issues, and to assess the degree to which we may really approach the limiting, idealized results.

6. More on Planetary Spectra

The cross-correlation techniques depend critically on the nature of the planet’s spectrum for their effectiveness. We consider therefore a number of aspects of planet spectra that bear on this but which may eventually lead to important new scientific information on the nature of the planet as one might go to higher spectral resolution with future very large aperture planet characterization missions or ground based projects.

All other things being equal, it is best to use the highest spectral resolution possible for a given bandpass constraint. The degree of structure, spectral variance, and of course scientific information such as relative line strengths always increases as spectral resolution increases. Even though the signal from the planet can be quite low, that of the star is typically high, and so we do not lose to detector readnoise as we would in a more conventional high resolution observation. As above, § 2, detector readnoise is one of the parameters entering concept designs and viable observing strategies.

As higher spectral resolutions are used, cross-correlation with a matched template more precisely locates the velocity of the planet. Monitoring of line locations allows not only discrimination against chromospheric activity on the host star but vital information on the orbit of the planet, and in turn on the mass of the planet. At the highest spectral resolutions, planetary emission features may become visible from night and day-glow lines as well as aurorae. If we can get into this regime, a new suite of diagnostics becomes available and detection can be optimised as lines would typically be extremely narrow, in contrast to the underlying relatively smooth stellar continuum.

The width of the correlation function (or equivalently absorption or emission line features in the planet’s atmosphere) contains additional information, from random thermal velocities as temperature indicators, to systematic line broadening due to the spin of the planet in its daily cycle.

As with most other time series observations of planets, we would expect to probe periodicities in intensities induced by the planets diurnal cycle. Ford, Seager and Turner (2001) discuss large albedo changes that may be recognizable in photometric observations of planets. If both the spin rate of the planet and the length of the day can be found, then we may estimate the geometric size of the planet.

On a longer term, yearly seasonal changes may be sought and changes due to “solar” cycles on even longer timescales. Atmospheric emission lines are especially sensitive to many changing conditions, such as local weather or surface conditions and atmospheric instabilities. The terrestrial OH Meinel system in the near-IR, for example, is intimately related to the chemistry of the terrestrial ozone layer and changes completely between day and night (Zipf 1966, Le Texier et al 1989). Other atmospheric emission lines arise from oxygen, atomic and molecular, sodium and nitrogen and are, to varying degrees, diagnostics of the presence of life on Earth.

7. Conclusions

We have considered the use of integral-field spectroscopy together with coronagraphy as an interesting approach to planet *detection* as well as characterization. The concept is to acquire a datacube of images, each at a different wavelength, of a star with planets shining by reflected light of the star modified by the integrated albedo (or emission) of the planet. The star is presumed to be occulted by the coronagraph, however there remains significant leakage or stray light from the star that dominates the problem of finding extrasolar planets. A potentially effective compromise modification to an integral-field spectrograph would be construction of a spectral datacube using narrow-band filters sequentially or a long-slit moved perpendicular to its length.

In the limiting case where the spectrum of the host star is the same across the field of view (or a region of interest within the field of view), we may use pattern recognition techniques to find extrasolar planets within the noisy spectra of the field. This is effectively done with cross-correlation using matched templates that in turn offer scientific insight into the nature of the spectrum of the planet. The S/N of the cross-correlation approach is the S/N of the ideal imaging case multiplied by the standard deviation of the planet’s spectrum (normalized to unit mean), which leads to pressure to use higher spectral resolution. Substantial gains can be made in rejecting the systematic contamination from the host star. In this limiting case, we may also use a general analysis of variance approach to estimate whether there is any source within the field other than just the host star, irrespective of its spectrum.

A method is described which mathematically completely eliminates the parasitic emission from the host star, although not the Poisson noise of that emission. This technique uses Gram-Schmidt orthonormalization, with the stellar spectrum and planet’s template providing basis vectors from which orthonormal vectors can be constructed. The S/N of the Gram-Schmidt method is essentially the same as that of the cross-correlation technique, but

with the advantage that stray light is *completely* eliminated.

In the case where the optics are diffraction limited, although not necessarily perfect, we describe a quite different technique to remove the stray light from the star. We call this “spectral deconvolution”, applicable to space-based observation and perhaps some ground-based adaptive optics approaches. In the diffraction limit, the spatial scales of the parasitic emission are proportional to wavelength. By numerically adjusting the image scales in the datacube to that of a reference wavelength, the PSF changes with wavelength are much less dramatic. We can fit a low order spectral function at each pixel of the resampled (“shrunk”) datacube and subtract it to approach the Poisson noise limit. However since the planet now occupies many spatial pixels and only a limited spectral window in the resampled datacube, its contribution to the flux is overlooked by the fitting procedure. When the star-subtracted datacube is reconstructed back onto the original scale, the planet spectrum is realigned and the planet may be seen by collapsing the datacube in the spectral dimension to make an image. This method offers, with a single observation, essentially *Poisson limited detection capability*. At the same time, and as part of the discovery observation, it provides a spectrum of the extrasolar planet from the outset and suitable for scientific investigation into the composition of the extrasolar planet’s atmosphere and possible biomarkers.

The parameter space encompassed by integral-field spectroscopy with coronagraphic imaging is vast, covering spatial extent, spatial resolution, spectral coverage, spectral resolution for telescopes of various sizes both ground and space based. The technical and practical difficulties are non-trivial, and there is a great deal of work required to understand which regimes may be most effectively pursued with techniques similar to those described here, or with much more sophisticated pattern recognition techniques, yet the promise seems sufficiently high that we feel the effort is likely to be worthwhile. If these methods do prove practical, the design of future instruments, and perhaps even missions optimized for planet detection and characterization, may be influenced, since it not only improves detection capability, but at the same time and as part of the discovery observation itself, can offer vital information on the character of the planet’s spectrum, including the presence of biomarkers and evidence for life.

We thank Prof. R. Kurucz for information and discussion relating to the use of his Solar models. We also thank Prof. Lloyd Wallace for similar discussion concerning the empirical Solar atlases. We are exceedingly grateful to John Krist for his assistance in producing the simulated coronagraphic images, and to Mark Clampin and Rick White for insightful discussion of the techniques described.

- Bacon, R., Adam, G., Baranne, A., Courtès, G., Dubet, D., Dubois, J.P., Emsellem, E., Ferruit, P., Georgelin, Y., Monnet, G., Pécontal, E., Rousset, A., Sayède, F., 1995, *A& AS*, 113, 347.
- Beuzit, J.L., Mouillet, D., Le Mignant, D., 2000, ESO documents GEN-MAN-VLT-11620-1834, “ADONIS Coronagraph User Manual”
- Boccaletti, A., Moutou, C., Labeyrie, A., Kohler, D., Vakili, F., 1998, *A& AS*, 133, 395.
- Brown, T., 2001, *ApJ*, 553, 1006.
- Brown, R.A., Burrows, C.J., 1990, *Icarus*, 87, 484.
- Charboneau, D., Brown, T.M., Noyes, R.W., Gilliland, R., 2002, *ApJ*, 568, 377.
- Collier Cameron, A., Horne, K., Penny, A., Dick, J., 1999, *Nature*, 402, 751.
- Collier Cameron, A., Horne, K., Penny, A., Leigh, C., 2002, *MNRAS*, 330, 187.
- Des Marais, D.J., Harwit, M., Jucks, K., Kasting, J., Lunine, J., Lin, D., Seager, S., Schneider, J., Traub, W., Woolf, N., JPL Publication 01-008, “Biosignatures and Planetary Properties to be Investigated by the TPF Mission”
- Ford, E.B., Seager, S., Turner, E.L., 2001, *Nature*, 412, 885.
- Ftaclas, C., Nonnenmacher, A.L., Gruszczak, A., Terrile, R.J., Pravdo, S.H., 1994, *SPIE*, 2198, 1324.
- Itoh, Y., Takato, N., Takami, H., Tamura, M., 1998, *PASJ*, 50, 55.
- Karkoschka, E., 1994, *Icarus*, 111, 174.
- Karkoschka, E., 1998, *Icarus*, 133, 134.
- Kasting, J.F., 1996, *Ap& SS*, 241, 3.
- Krassovsky, V.I., Shefov, N.N., Yarin, V.I., 1962, *Planet Space Sci.* 9, 883.
- Kuchner, M.J., Traub, W.A., 2002, *ApJ*, May 2002; astro-ph/0203455.
- Larson, H.P., 1980, *ARAA*, 18, 43.
- Leinert, Ch., Bowyer, S., Haikala, L.K., Hanner, M.S., Hauser, M.G., et al. 1998, *A& ASupp*, 127, 1.
- Le Texier, H., Solomon, S., Thomas, R.J., Garcia, R.R., 1989, *Annales Geophysicae*, 7, 365.

Livingston, W., Wallace, L., 1991, NSO Technical Report #91-001, Tucson: National Solar Observatory, “An Atlas of the Solar Spectrum in the Infrared from 1850 to 9000 cm^{-1} ”

Maihara, T., Iwamuro, F., Yamashita, T., Hall, D.N.B., Cowie, L.L., Tokunaga, A.T., Pickles, A., 1993, PASP, 105, 940.

Marcy, G.W., Butler, R.P., 1998, ARAA, 36, 57.

Marois, C., Doyon, R., Racine, R., Nadeau, D., 2000, PASP, 112, 91.

Meinel, A.B., 1950, ApJ, 111, 207.

Olivia, E., Origlia, L., 1992, A& A, 254, 466.

Racine, R., Walker, G.A.H., Nadeau, D., Doyon, R., Marois, C., 1999, PASP, 111, 587.

Ramsey, S.K., Mountain, C.M., Geballe, T.R., 1992, MNRAS, 259, 751.

Roddier, F., Roddier, C., 1997, PASP, 109, 815.

Rouan, D., Riaud, P., Boccaletti, A., Clénet, Y., Labeyrie, A., 2000, PASP, 112, 1479.

Schindler, T.L., Trent, L., Kasting, J.F., 2000, Icarus, 145, 262.

Spiegel, D., Kasdin, J. 2001, AAS, 199, 8603.

Tokunaga, A.T., Knacke, R.F., Ridgway, S.T., Wallace, L., 1979, ApJ, 232, 603.

Tonry, J., Davis, M., 1979, AJ, 84, 1511.

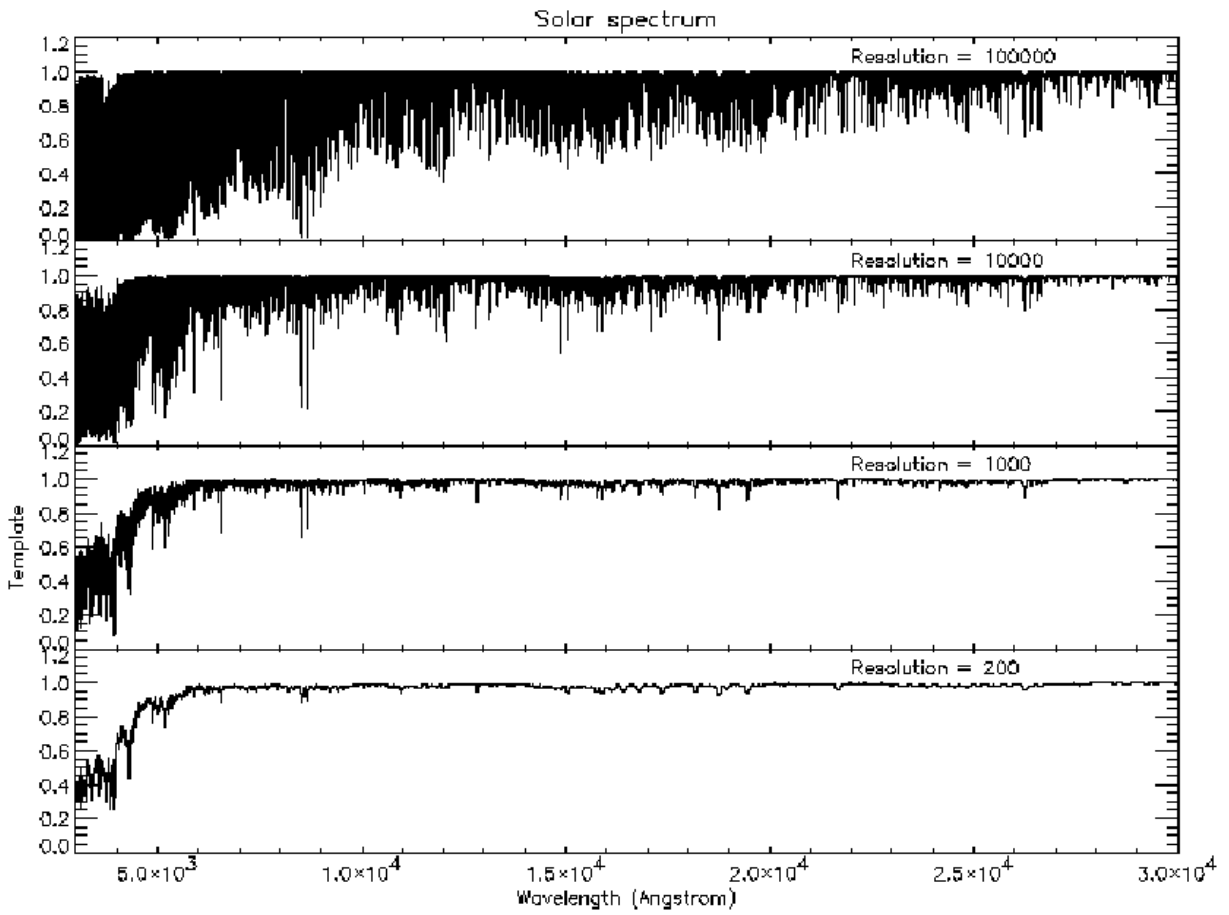
Wallace, L., Hinkle, K., Livingston, W., 1993, NSO Technical Report #93-001, Tucson: National Solar Observatory, “An Atlas of the Photospheric Spectrum from 8900 to 13600 cm^{-1} ”

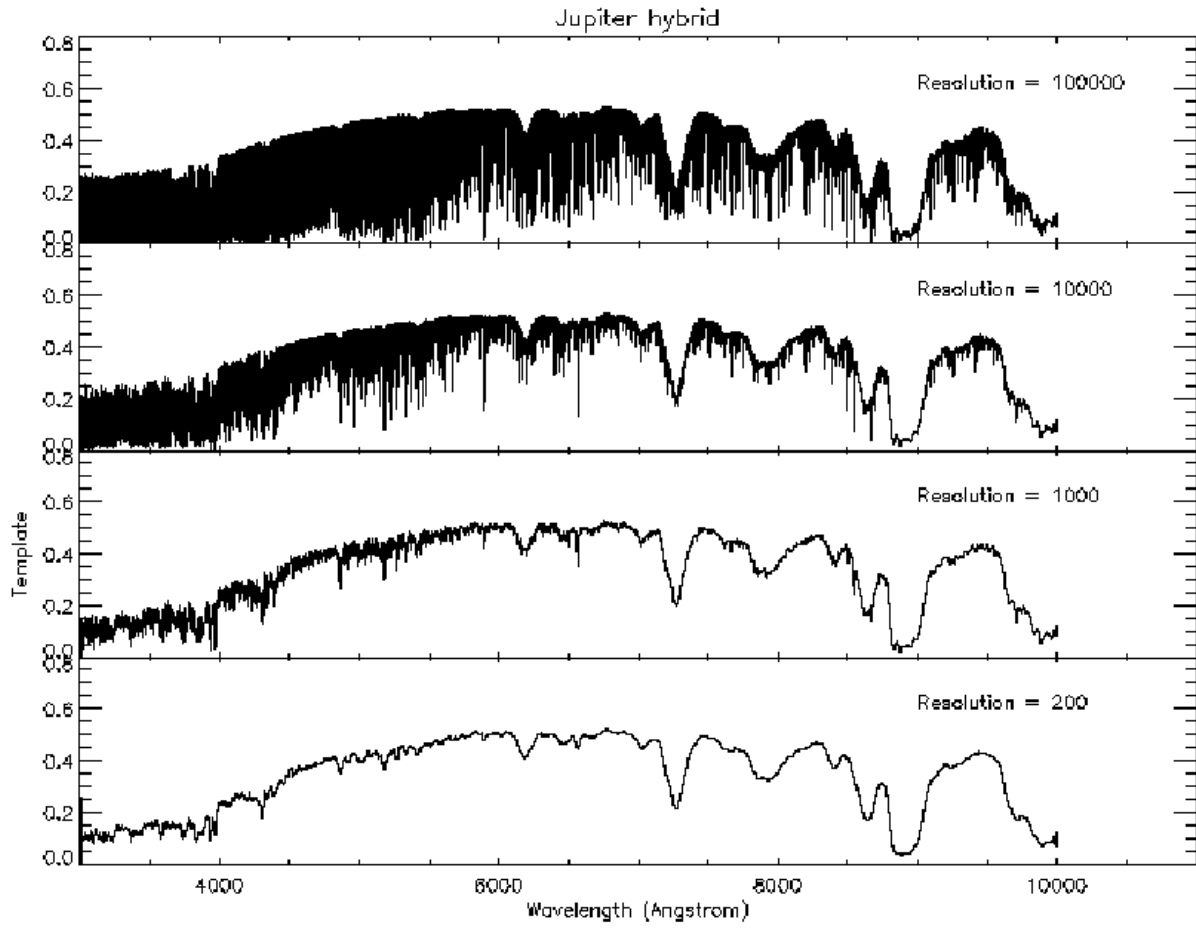
Wallace, L., Hinkle, K., Livingston, W., 1998, NSO Technical Report #98-001, Tucson: National Solar Observatory, “An Atlas of the Spectrum of the Solar Photosphere from 13,500 to 28,000 cm^{-1} ”

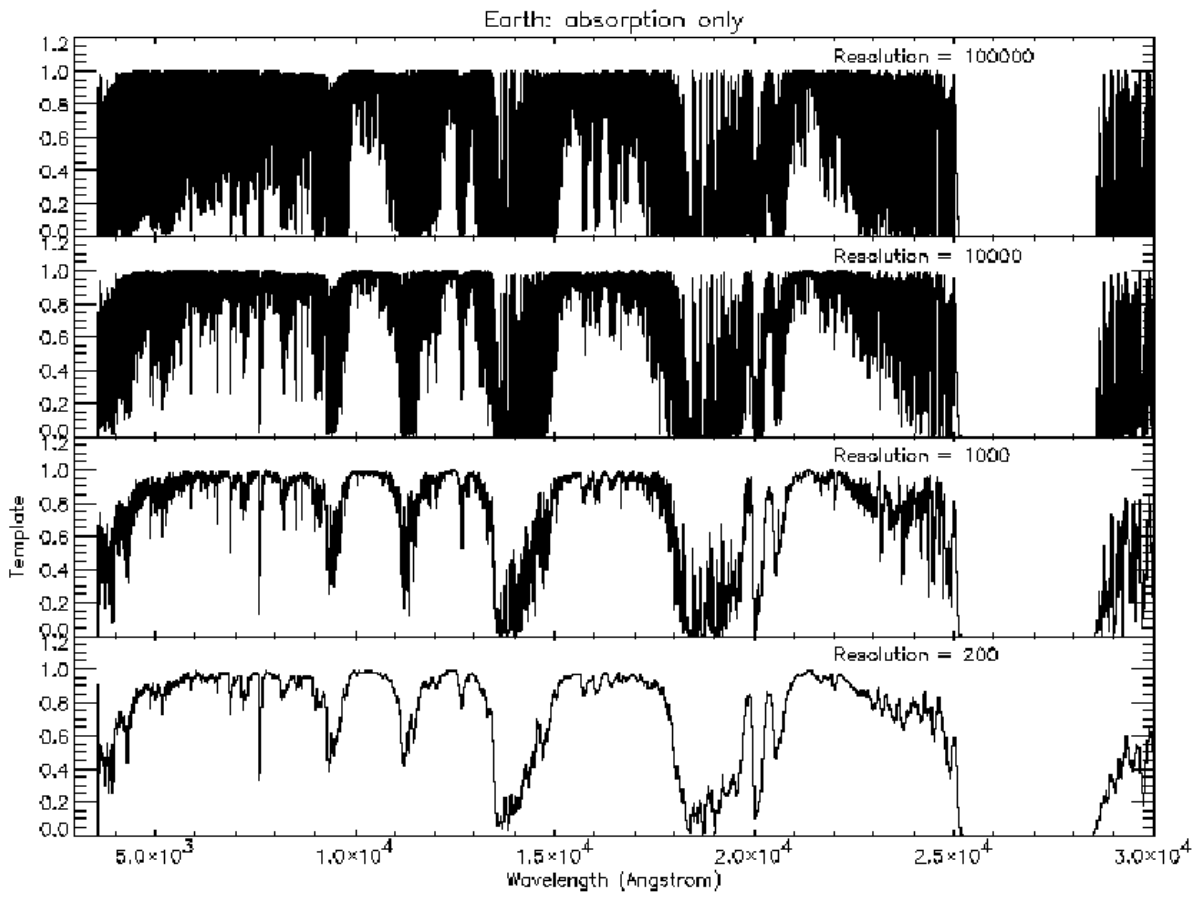
Wolf, N., Angel, J.R., 1998, ARAA, 36, 507.

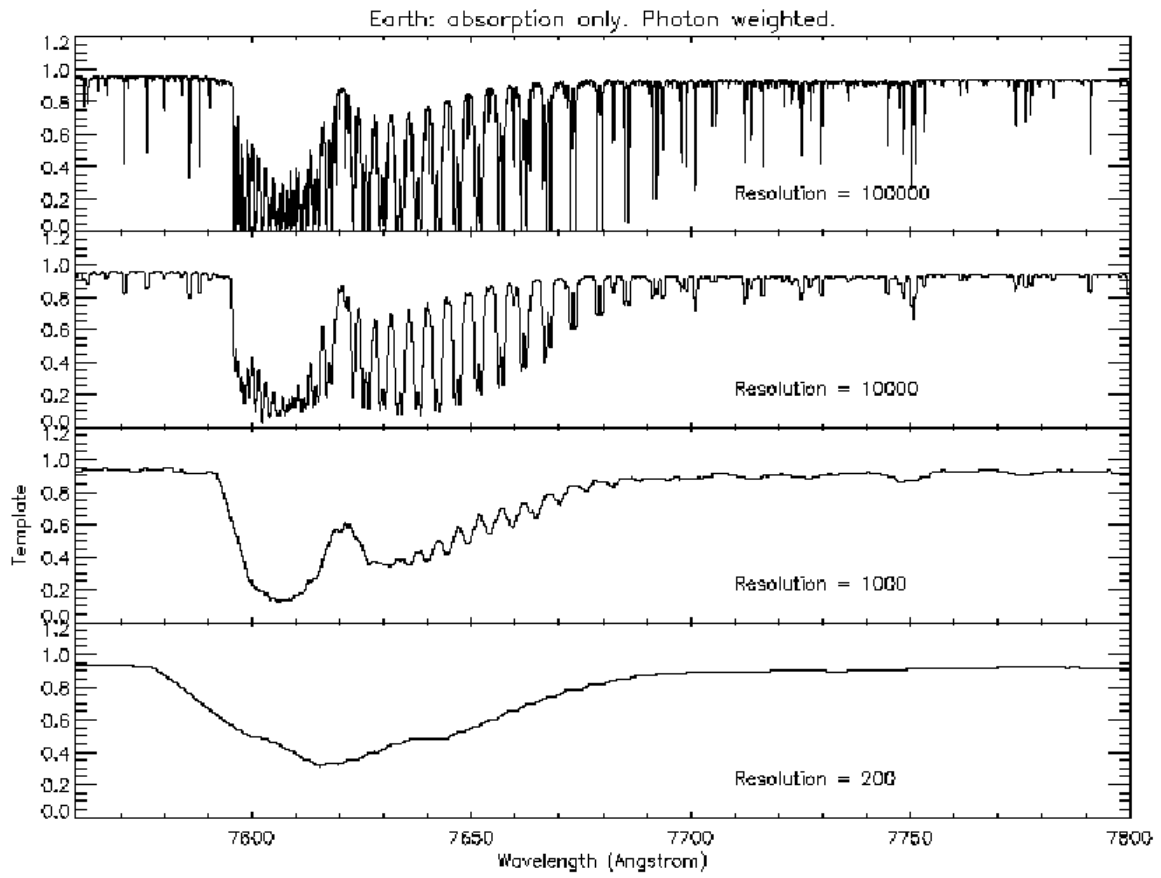
Wolf, N.J., Smith, P.S., Traub, W.A., Jucks, K.W., 2002, ApJ, in press; astro-ph/0203465

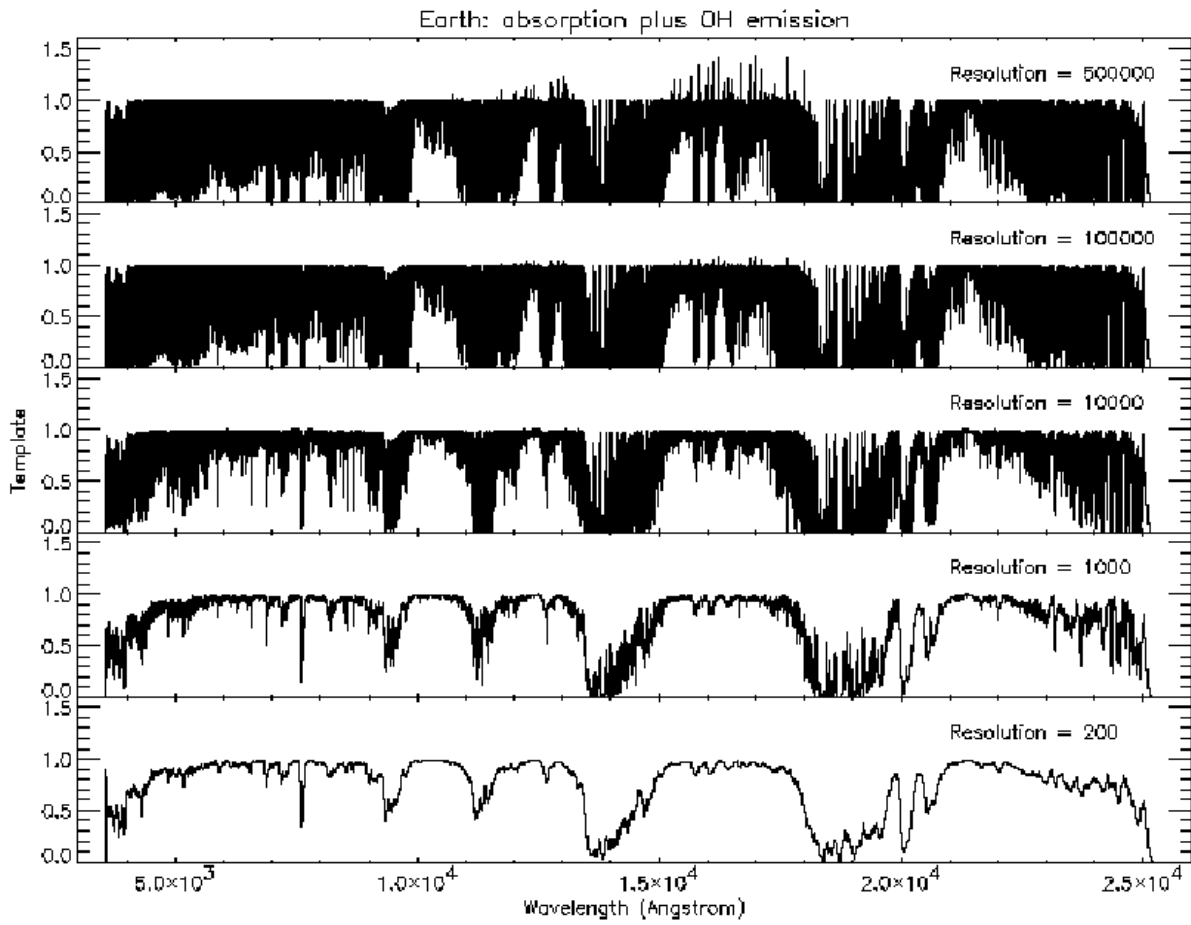
Zipf, E.C., 1966, J. Geomag. and Geoelec, 18, 301.

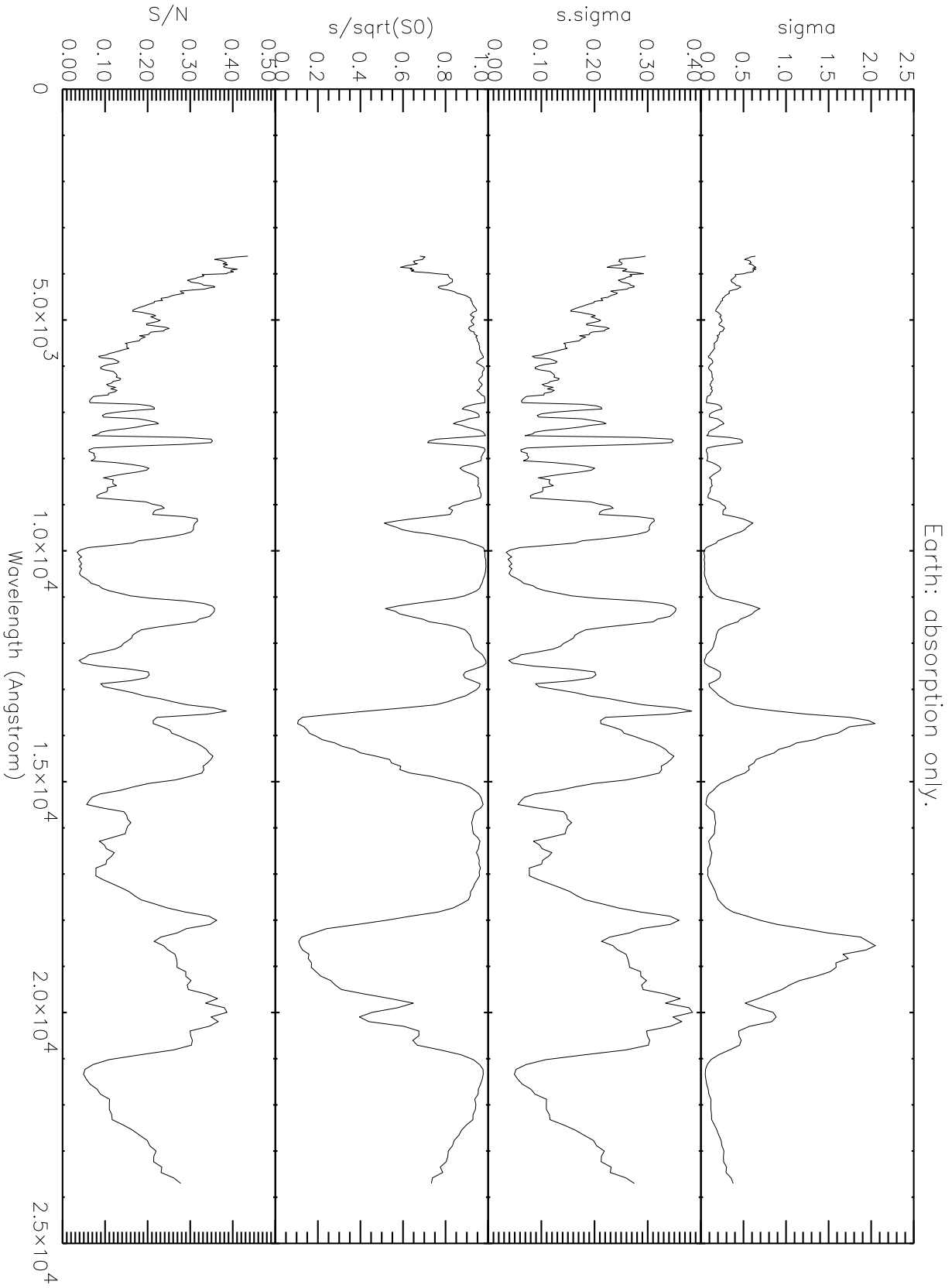


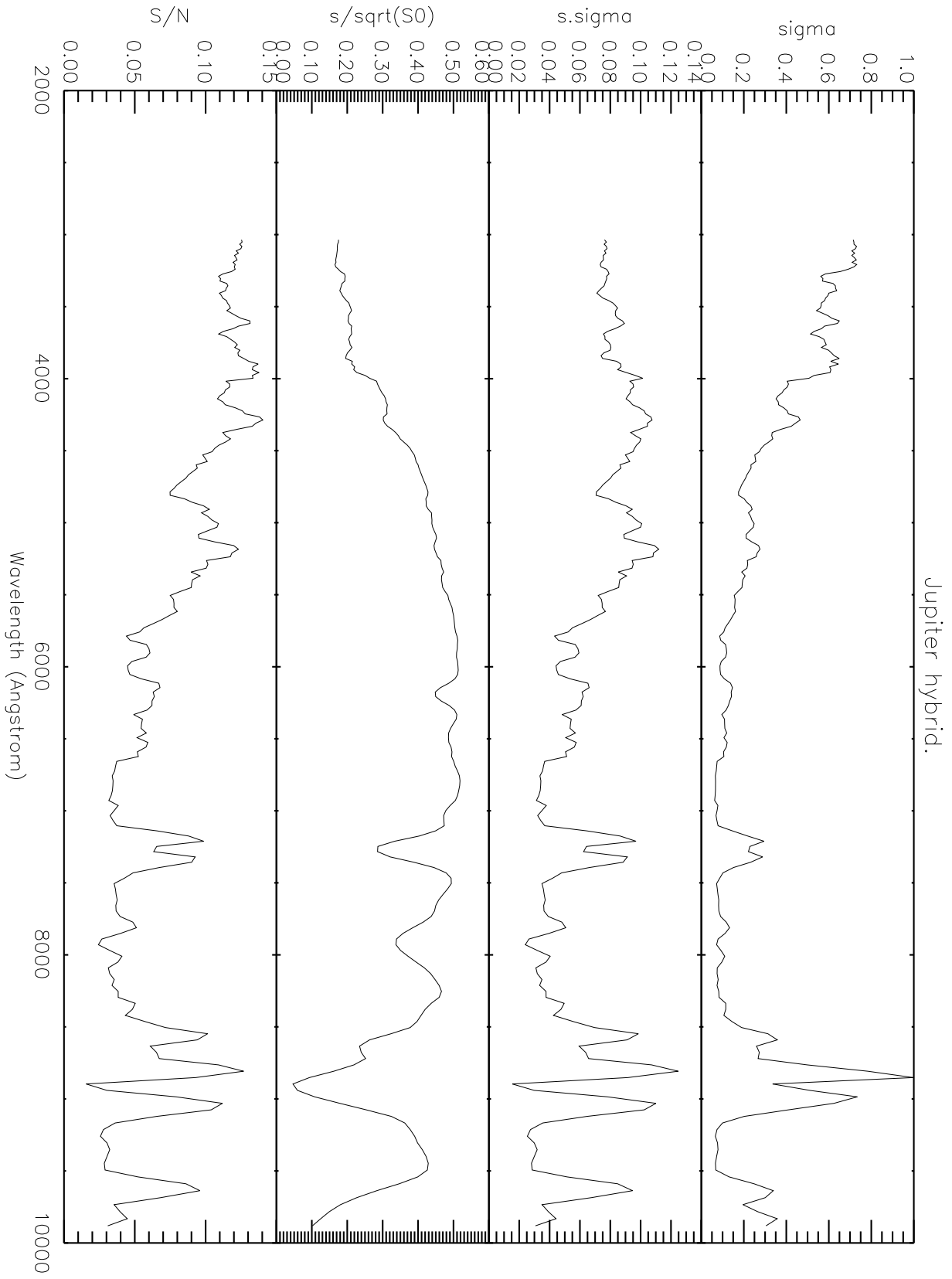


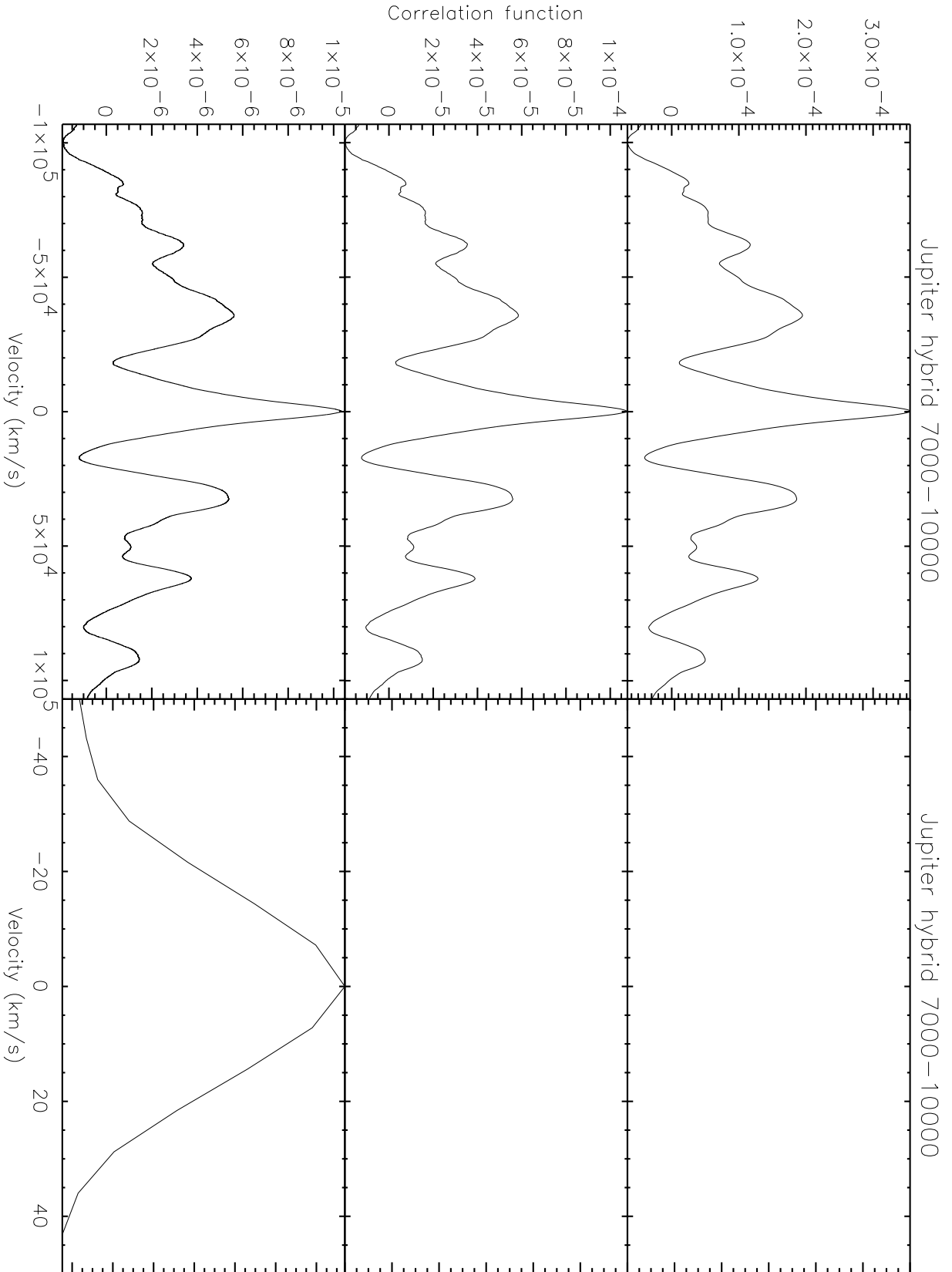




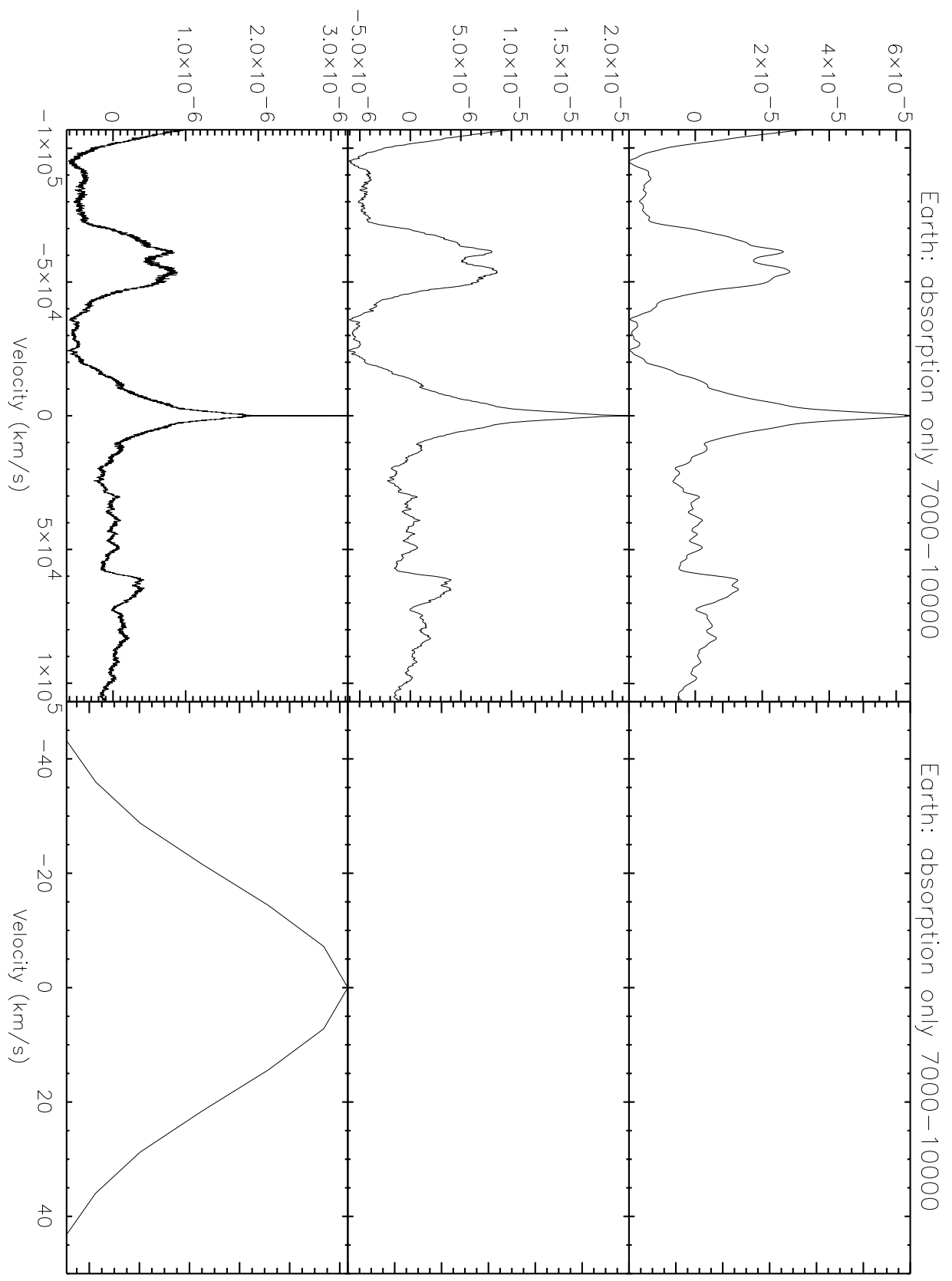


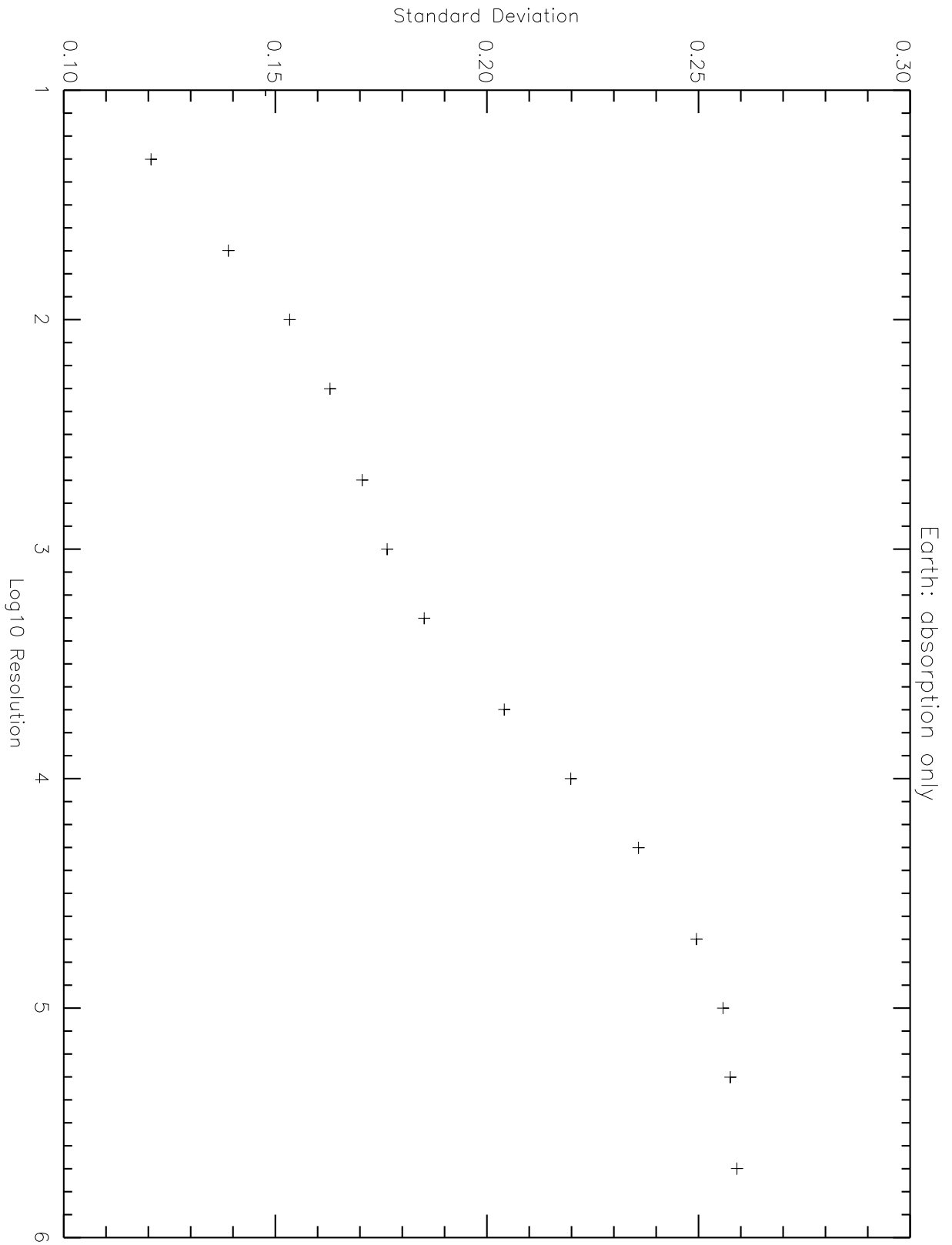


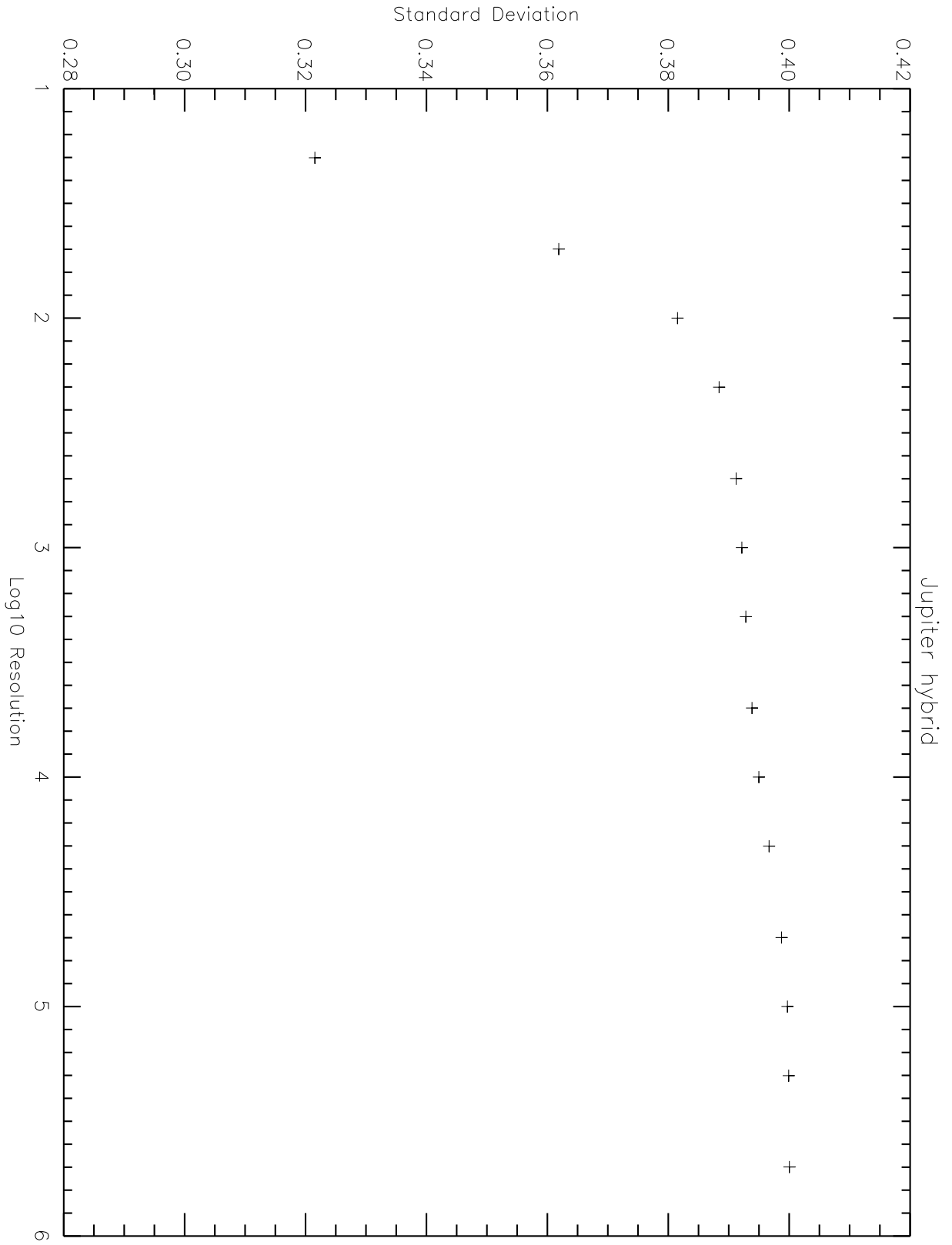


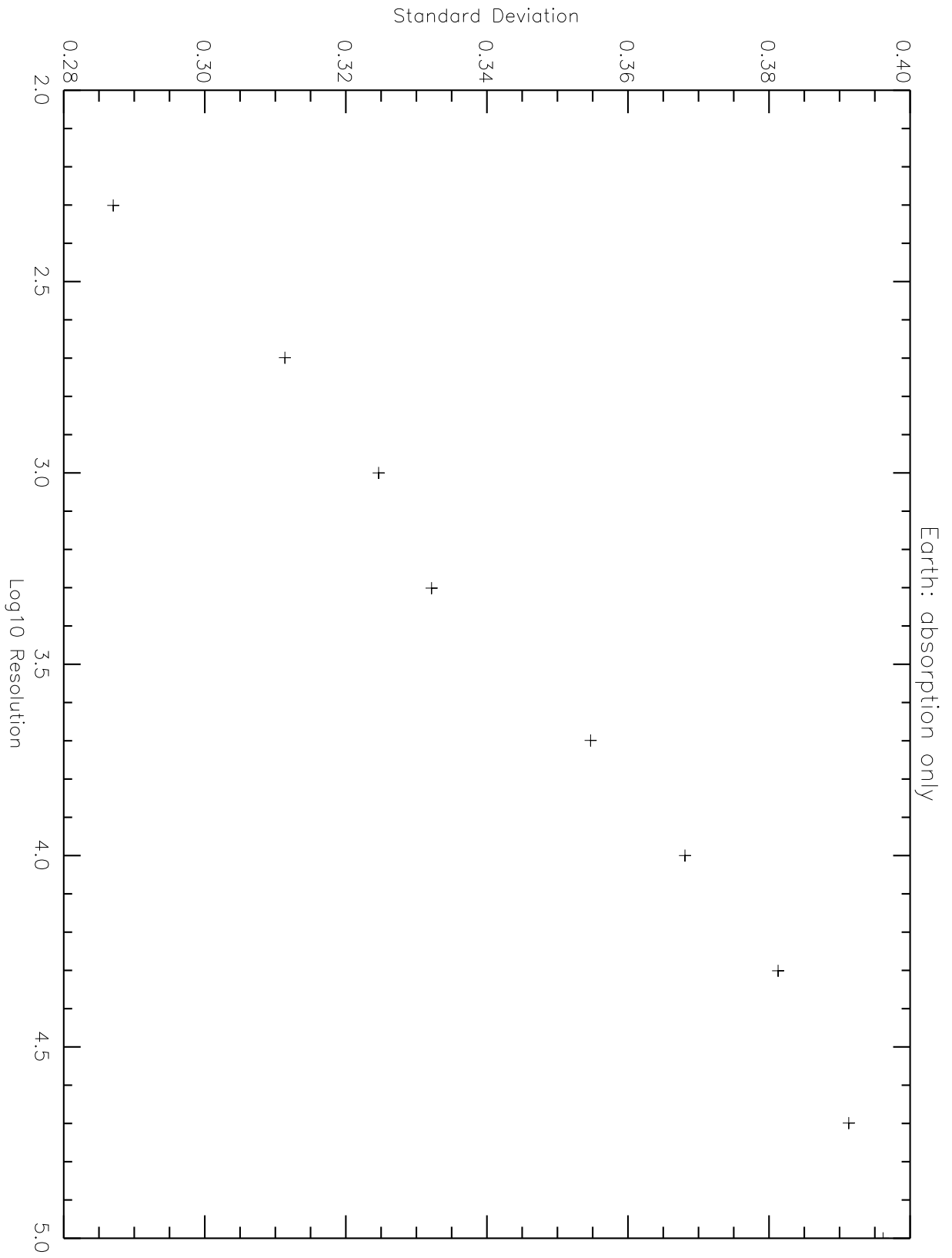


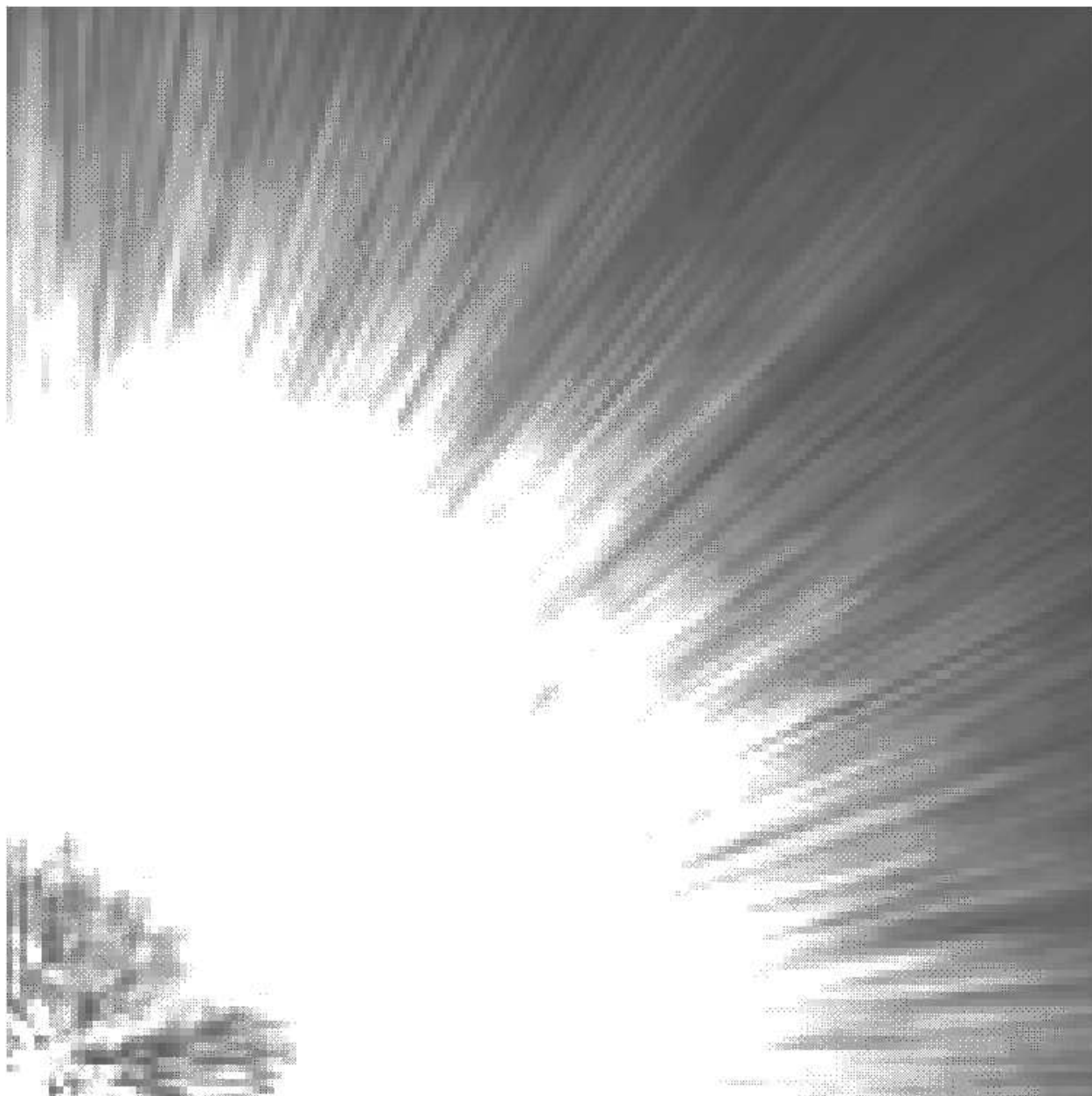
Correlation function



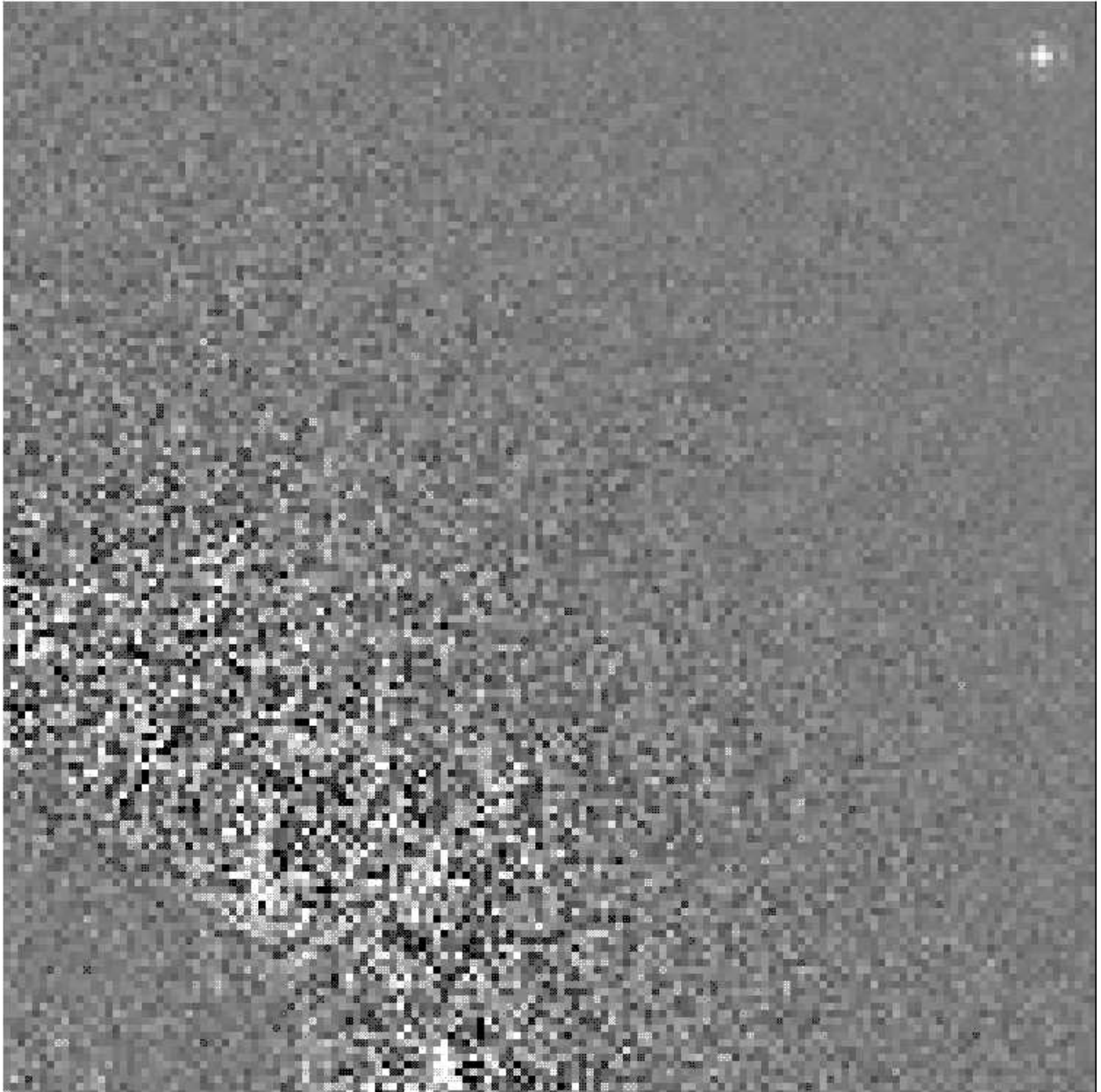


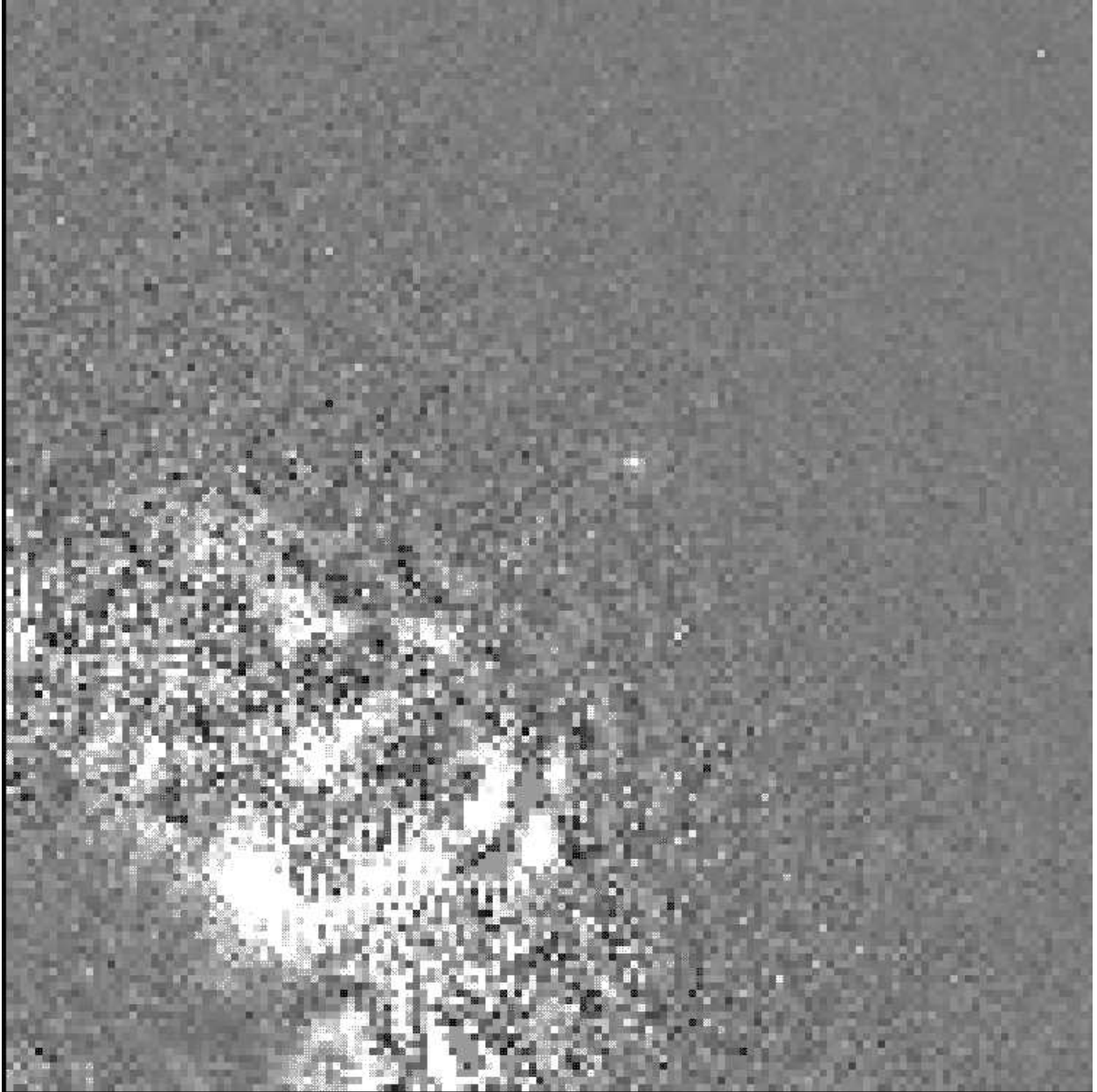


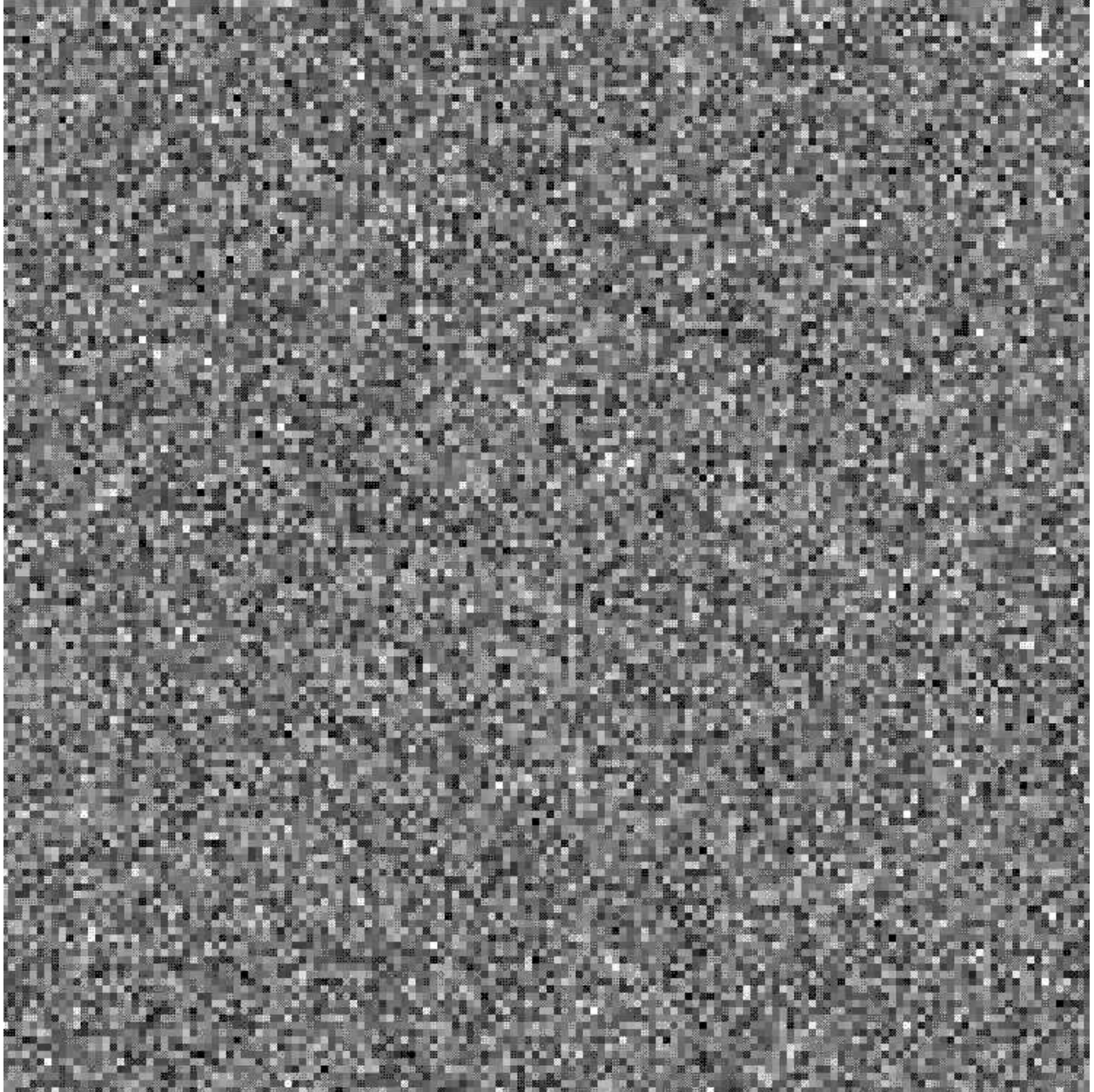














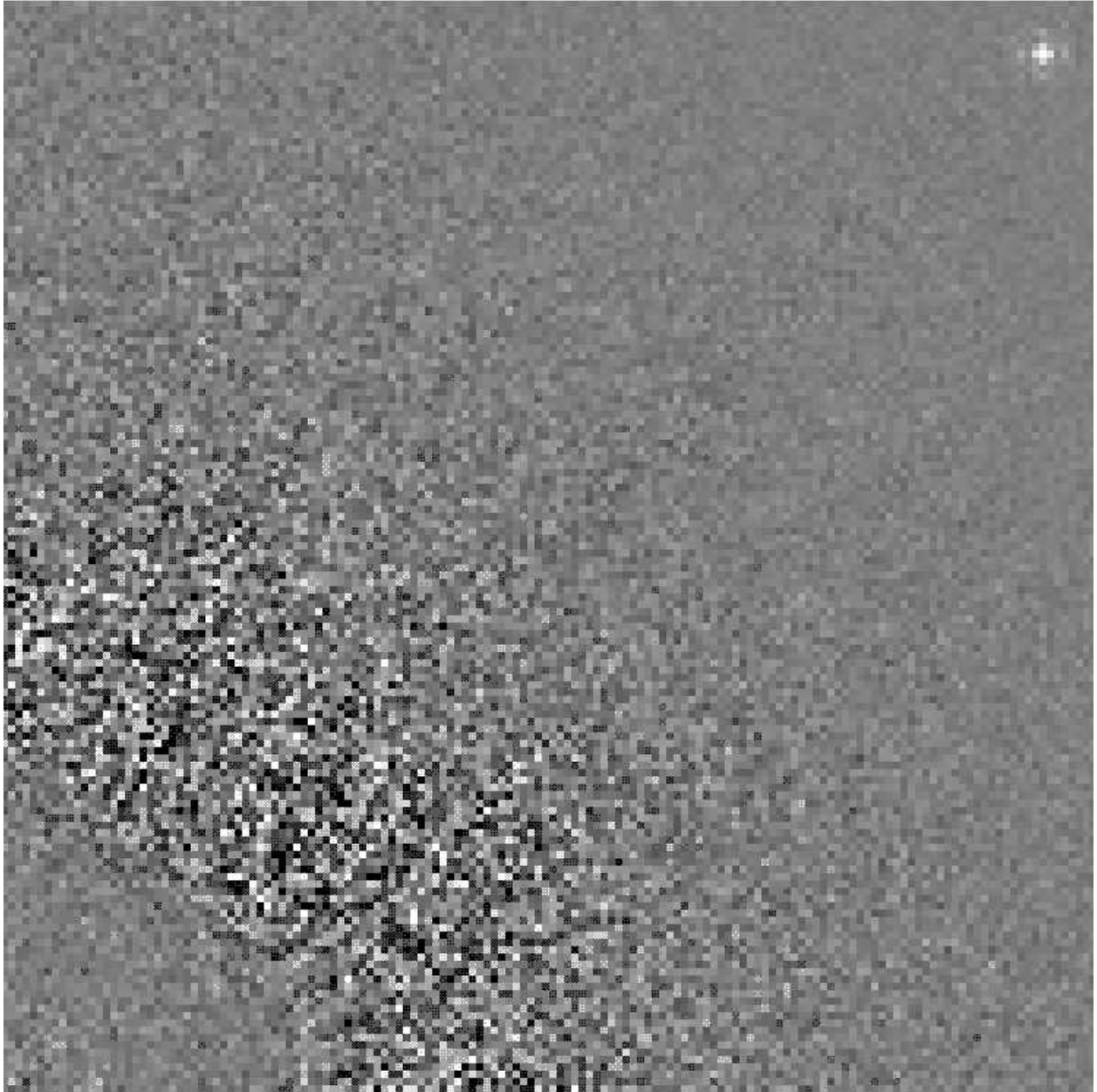


Fig. 1.— Solar spectrum, continuum normalized, showing the growth of structure as spectral resolution increases. Although the spectra in this plot and the following are plotted against wavelength, the actual underlying sampling is logarithmic. The resolution is as indicated in the panels.

Fig. 2.— Hybrid Jovian template constructed from high resolution Solar model multiplied by moderate resolution Jovian albedo spectrum, Karkoschka (1994).

Fig. 3.— Terrestrial template obtained by multiplying the high resolution Solar model by the square of the atmospheric transmission functions of the empirical Solar atlases described in the text.

Fig. 4.— Detail from the previous figure, showing the oxygen A-band absorption feature, and the growth of fine structure as the spectral resolution is increased.

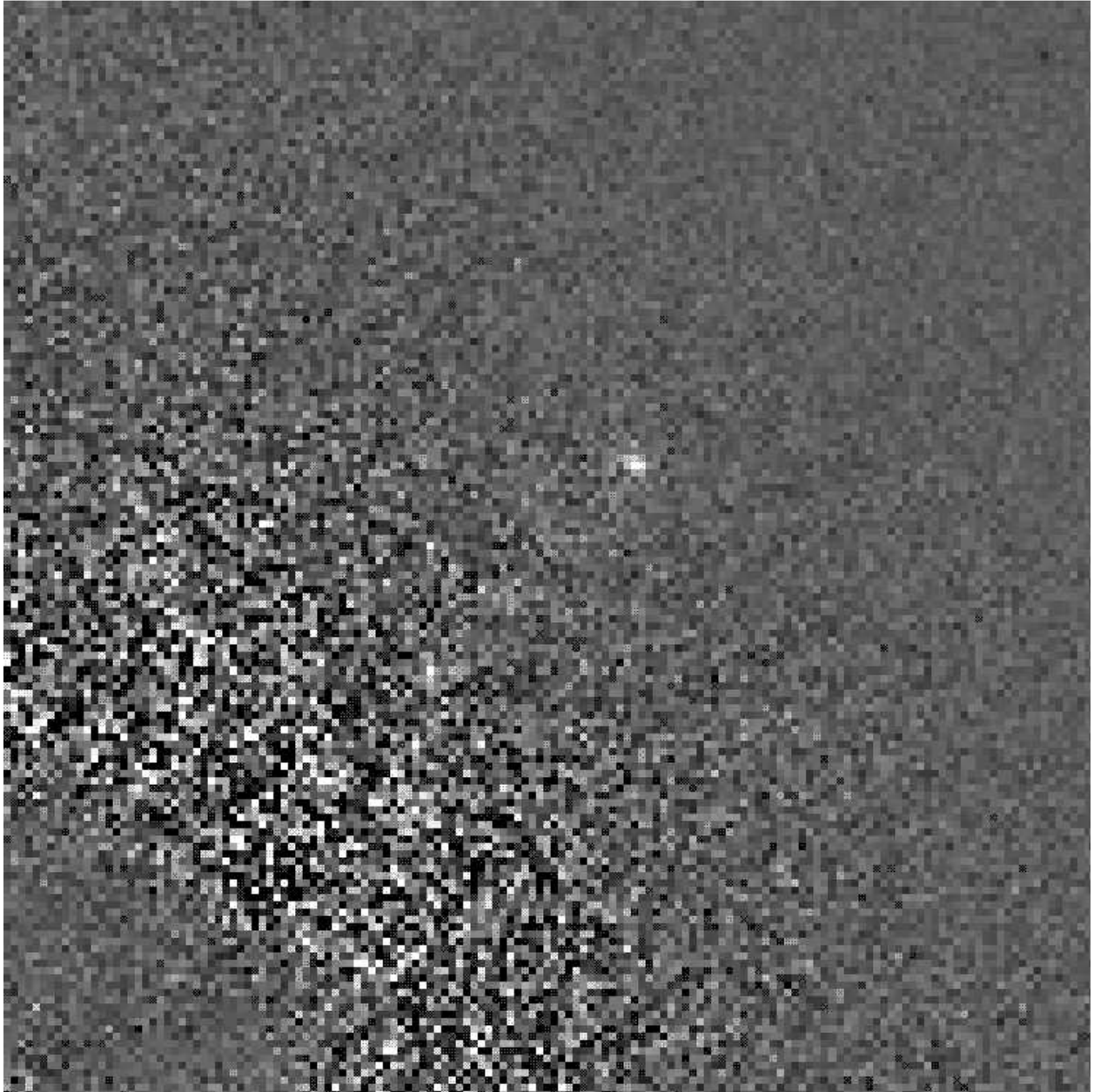
Fig. 5.— Similar terrestrial template to Fig. 3, but now with OH emission lines in the region $1\mu m - 2\mu m$ added as described in the text to assess their observability at high resolution.

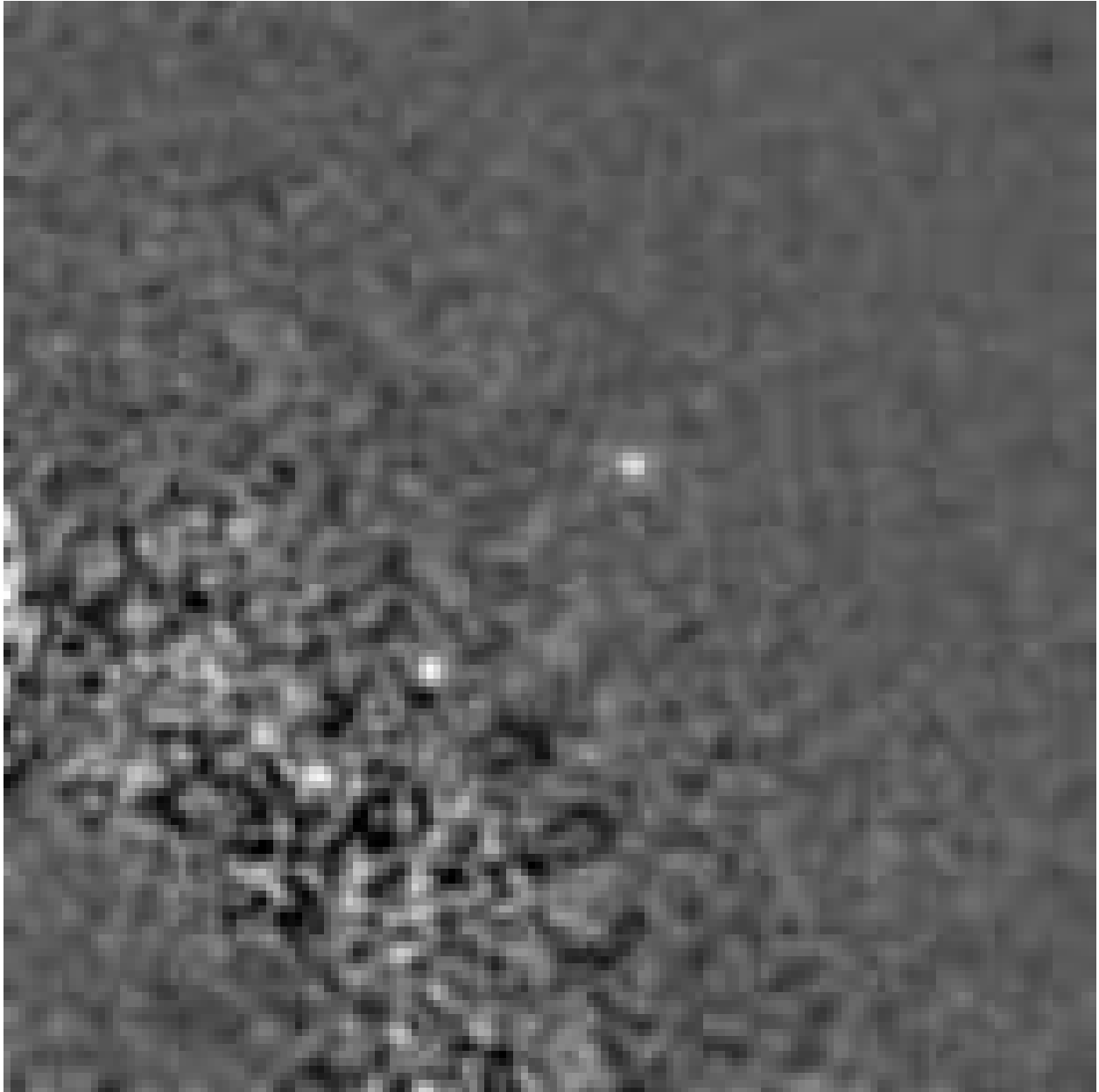
Fig. 6.— For a spectral window 2% of the wavelength in question, we plot the cross-correlation detectability parameters (Equ. 5) in various combinations as a function of wavelength for the terrestrial template. The top panel plots the standard deviation of the unit-mean template, σ , the second panel is the product $s_p\sigma$ with s_p from the template. The third panel is $s_p/\sqrt{S_0}$ with S_0 from the stellar template, and the bottom panel the final $S/N = s_p\sigma/\sqrt{S_0}$.

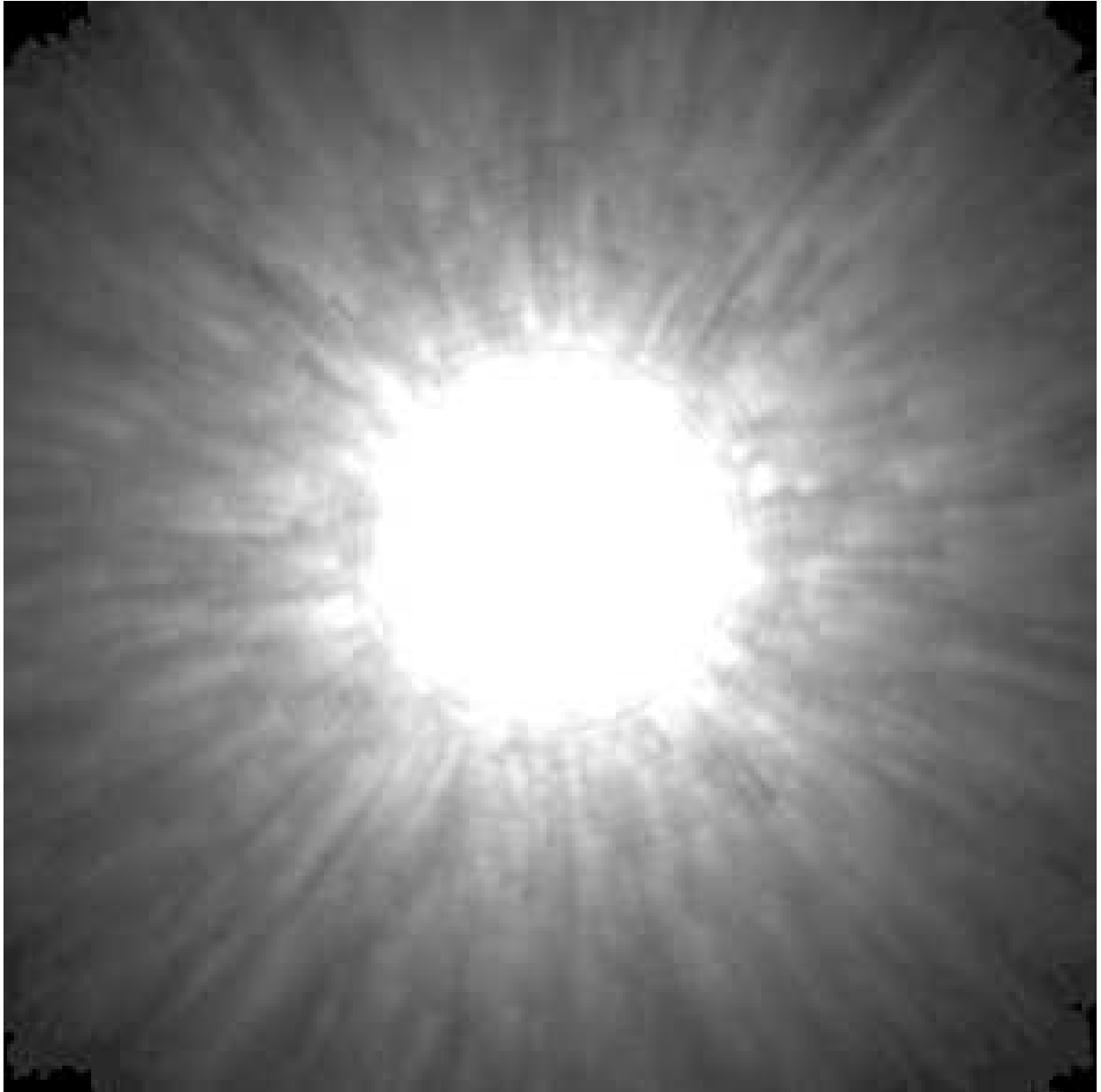
Fig. 7.— For a spectral window 2% of the wavelength in question, we plot the cross-correlation detectability parameters as a function of wavelength for the Jovian template with panels as in the caption to Fig. 6.

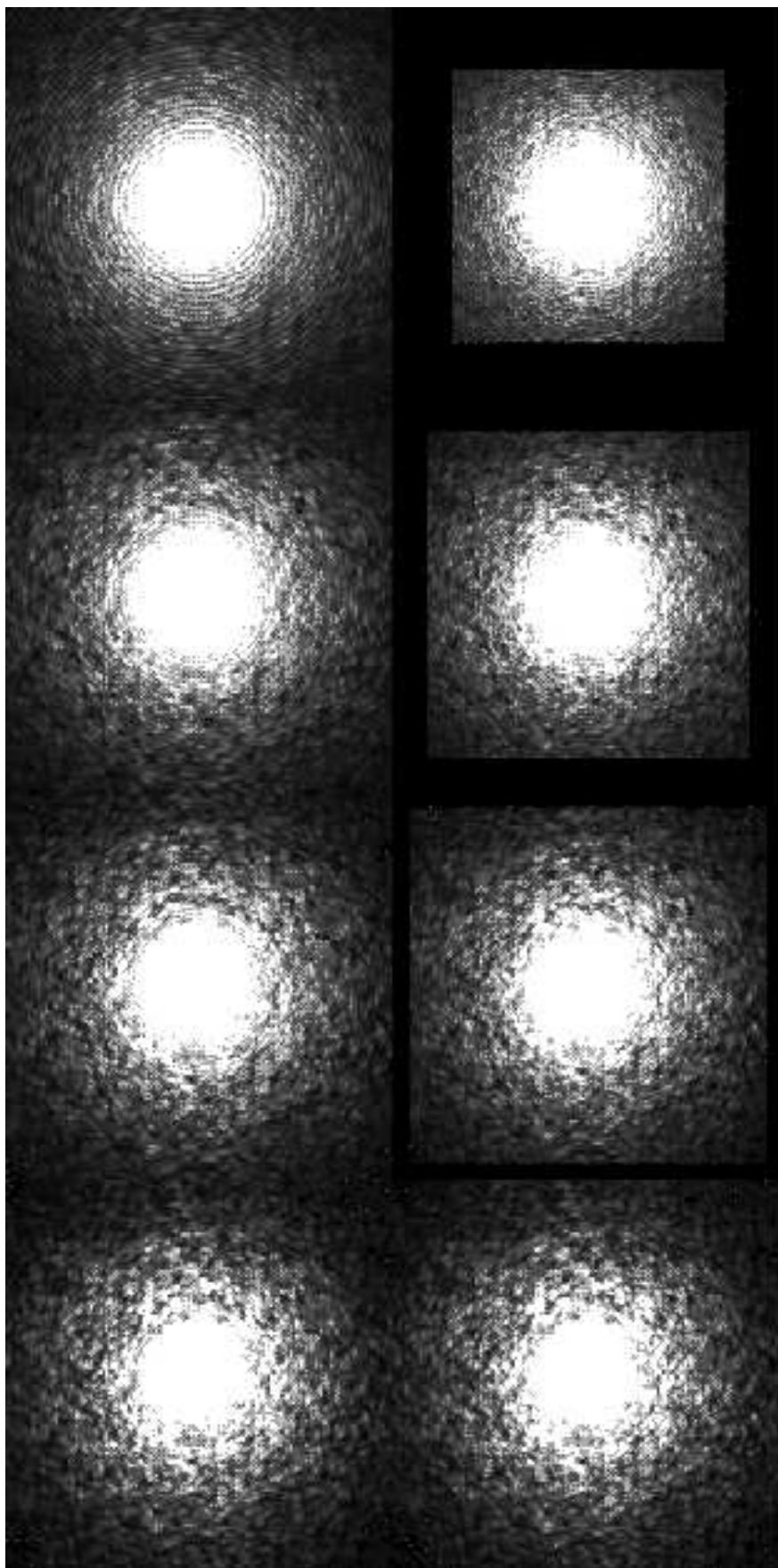
Fig. 8.— Noiseless autocorrelation function for the Jovian template in the wavelength region $7000\text{\AA} - 10,000\text{\AA}$ as a function of spectral resolution. The top, center and bottom panels are for spectral resolution 300, 1000 and 10,000 respectively. There is a minor increase in the sharpness of the autocorrelation function as the resolution is increased, but most of the power in the spectrum comes from the broad, diffuse bands (which may be an artifact of the template construction). The right hand column expands the velocity scale, intended to show the high resolution case autocorrelation peak.

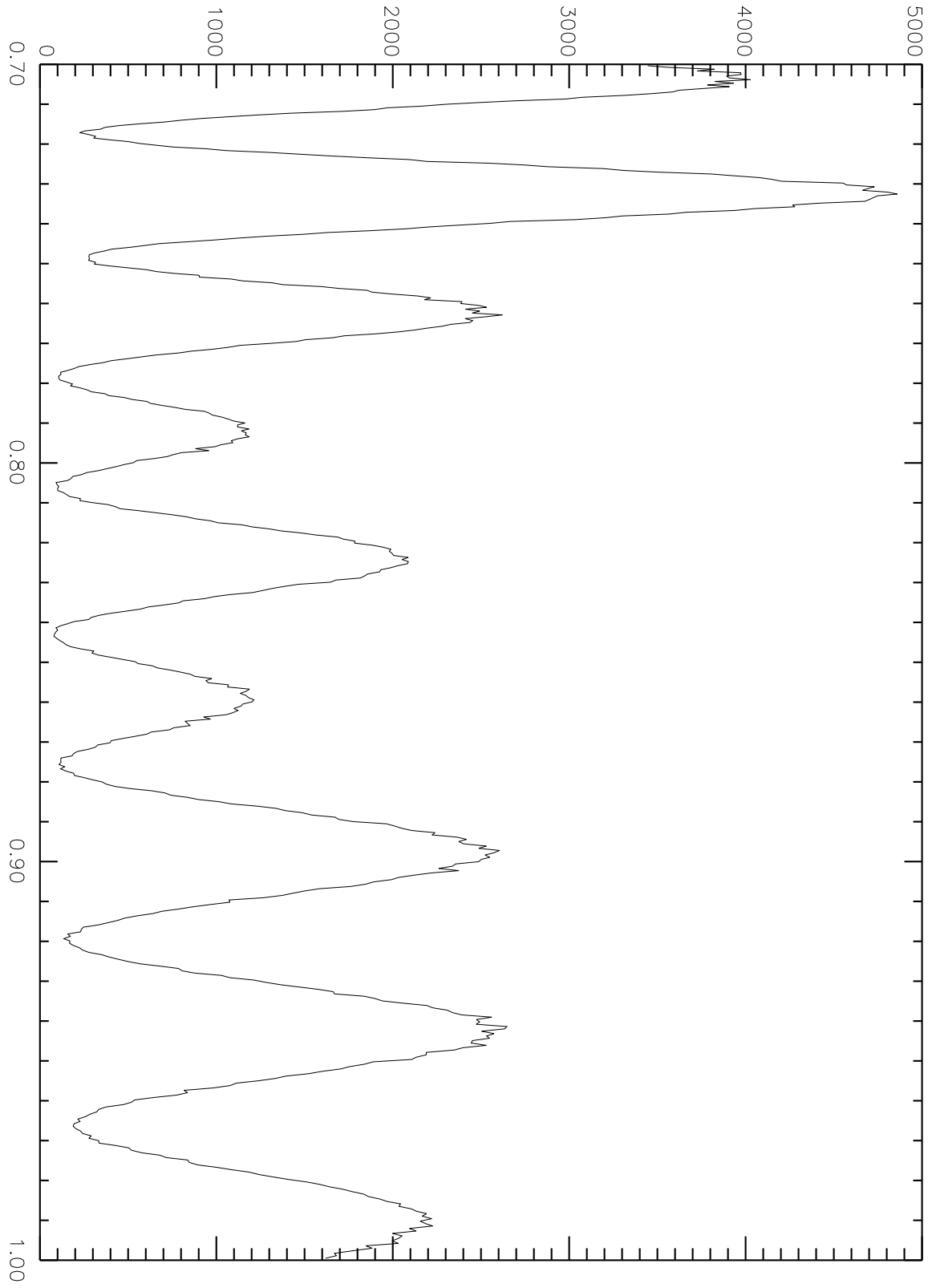
Fig. 9.— Noiseless autocorrelation function for the terrestrial template in the wavelength region $7000\text{\AA} - 10,000\text{\AA}$ as a function of spectral resolution. The top, center and bottom panels are for spectral resolution 300, 1000 and 10,000 respectively. Because of the dominance of fine structure in the terrestrial spectrum, the autocorrelation becomes very finely peaked

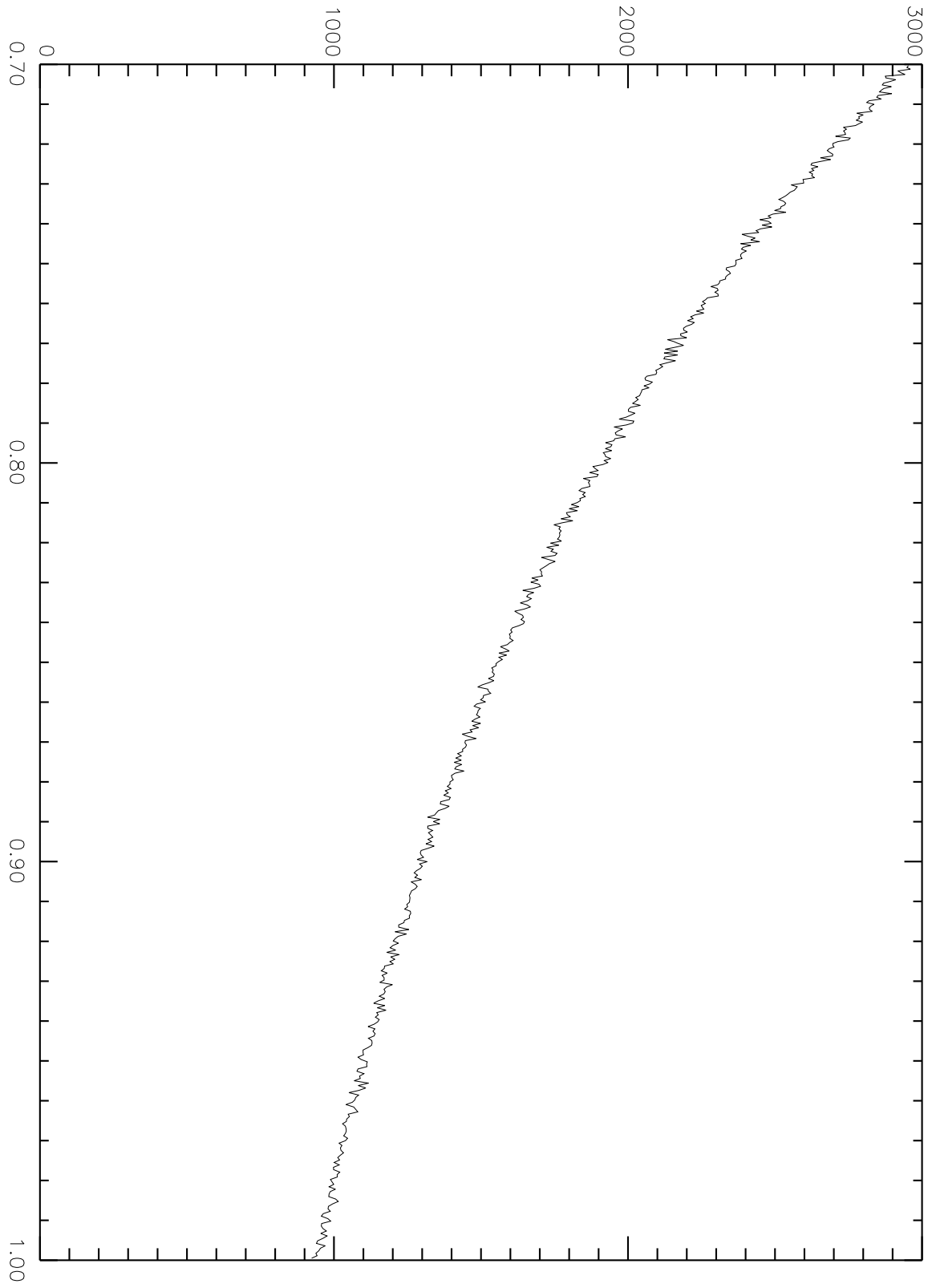


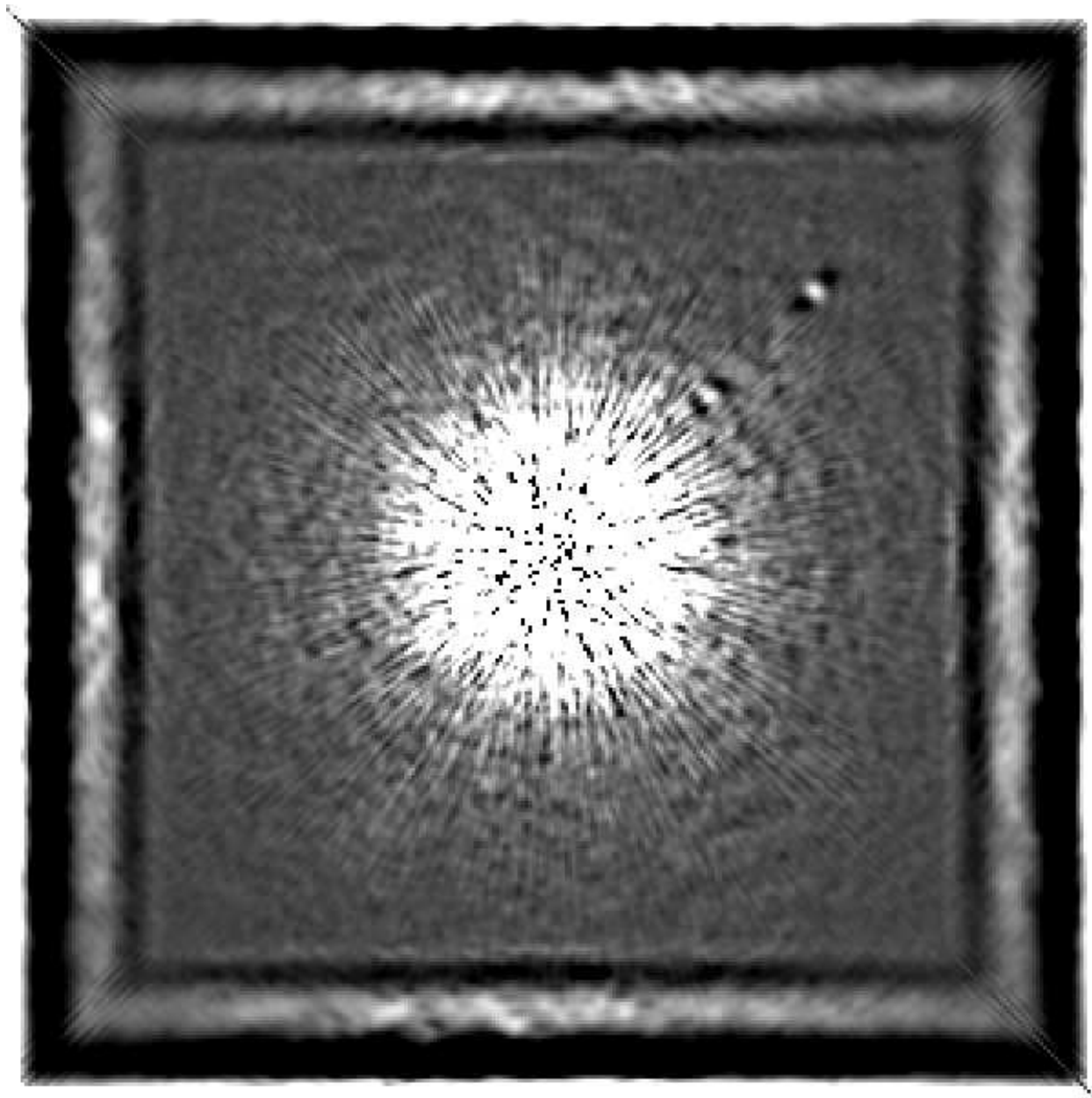


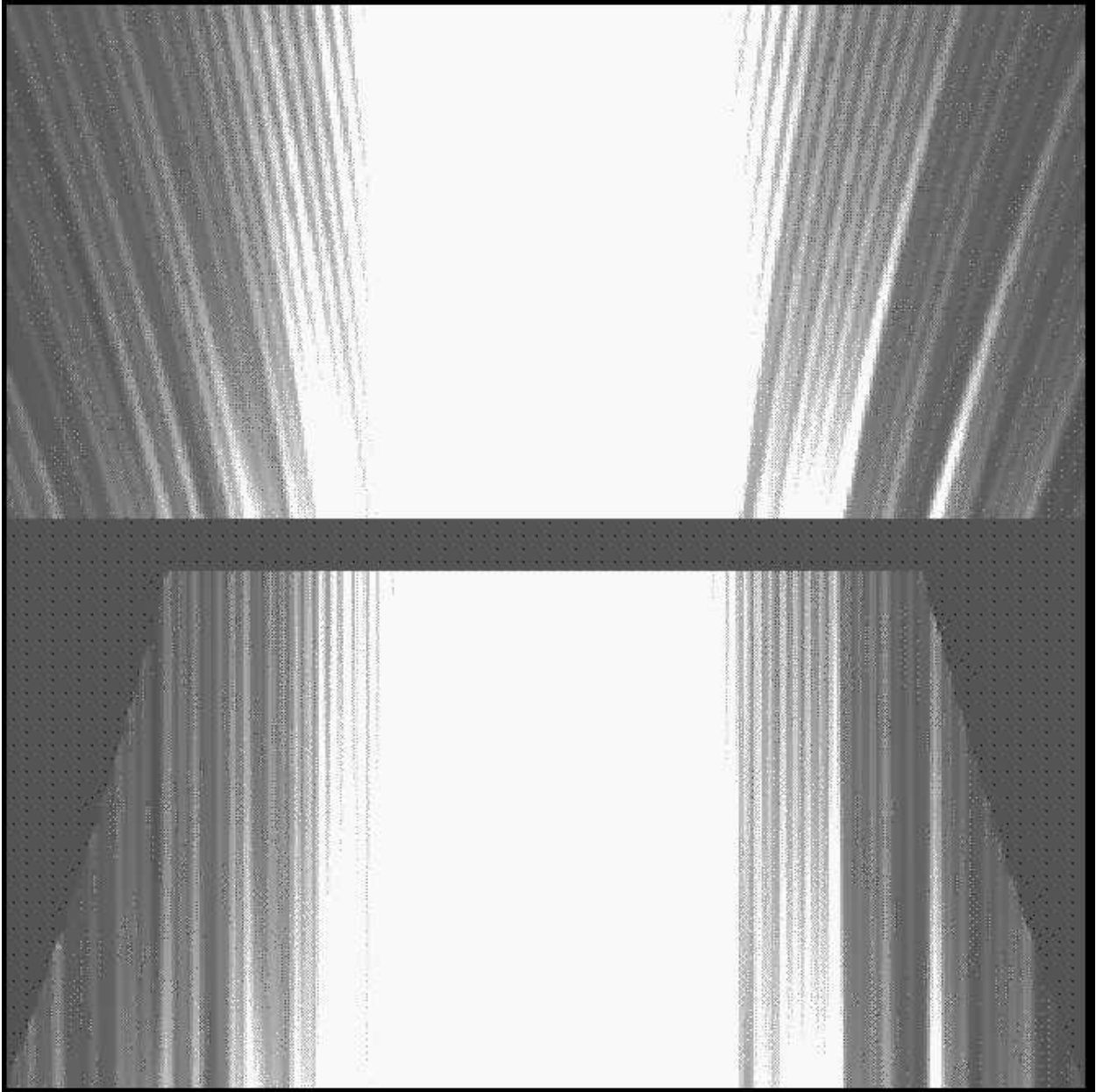












in the high resolution case. As in Fig. 8, the right hand column expands the velocity scale about the autocorrelation peak to illustrate the accuracy of velocity measurement that might be achieved.

Fig. 10.— Dispersion of the unit-mean template as a function of spectral resolution for the terrestrial template from 7000Å to 10,000Å. Note the continuous rise in σ due to the presence of fine structure in the spectrum.

Fig. 11.— Dispersion of the unit-mean template as a function of spectral resolution for the Jovian template. The standard deviation ceases to rise at resolutions above ≈ 300 as the majority of power in this template lies in the diffuse molecular band features. This may be an artifact of the template.

Fig. 12.— Dispersion of the unit-mean template as a function of spectral resolution for the terrestrial template from 7580Å to 7800Å, corresponding to a spectral region including the oxygen A-band complex. The high level of complexity in this feature causes the standard deviation to rise continuously with resolution.

Fig. 13.— Simulation of realistic coronagraphic image obtained using the ACS aberrated beam coronagraph showing typical PSF wings and is intended to provide a generic representation of PSF complexity that might be encountered.

Fig. 14.— Simulation of a “roll deconvolution” in which a pair of coronagraphic images obtained at different roll angles have been subtracted from one another. Slight miscenterings and focus changes (breathing) were introduced between the two. There is a Jovian planet visible in the top right corner.

Fig. 15.— Correlation function, c_0 , for the roll-deconvolved datacube using the hybrid Jovian template. The Jovian planet is clearly visible in the top right corner.

Fig. 16.— Correlation function for the roll-deconvolved datacube using the terrestrial template. The “bright Earth” is clearly visible.

Fig. 17.— Analysis of variance image showing an image of reduced- χ^2 with a peak at the location of the Jovian planet, and a second at the inner position of the “bright Earth”.

Fig. 18.— Image of the probability associated with reduced- χ^2 thresholded at $5 - \sigma$ showing a statistical signature of both planets.

Fig. 19.— Gram-Schmidt correlation function image using the Jovian template applied to the original (not roll-deconvolved) coronagraphic datacube. The Jovian planet is clearly

visible, and the remainder of the image shows only noise expected from photon statistics.

Fig. 20.— Gram-Schmidt correlation function image using the terrestrial template applied to the original (not roll-deconvolved) coronagraphic datacube. The outer bright-Earth planet is clearly visible.

Fig. 21.— Lightly smoothed version of the previous figure, showing all three inner planets. Note that the outer Jovian planet does not appear.

Fig. 22.— Simulation of space-based coronagraphic observation of Solar type star at a distance of 2 pc over the wavelength range 7000\AA to $1\mu\text{m}$, with parameters as given in the text. The figure shows the spectrally integrated PSF, representative of a direct image taken with an I-band filter.

Fig. 23.— Sequences showing cuts through the datacube at wavelengths $0.70\ \mu\text{m}$, $0.76\ \mu\text{m}$, $0.84\ \mu\text{m}$ and $1.0\ \mu\text{m}$, bottom to top, The left four panels show the speckles and ripples expanding with wavelength. The right panels illustrates the process of adjusting image scale as a function of wavelength, and PSF features can now be seen to remain fixed in place.

Fig. 24.— Spectral plot for a pixel near the Jovian planet in the original datacube showing strong modulation as Airy rings and speckles move across the pixel.

Fig. 25.— Spectral plot for the same pixel in the scale-adjusted datacube showing the removal of rapid modulation and only low frequency terms which are easily modelled.

Fig. 26.— Spectrally collapsed image of the reconstructed, subtracted datacube showing a 20σ detection of a Jovian planet whose peak is only 1% of the PSF wing background, using a 2-m telescope. The equivalent observation with an 8-m TPF would correspond to a terrestrial scale planet.

Fig. 27.— Cuts through the original datacube with one spatial and one spectral dimension. In the original cube, the rings diverge outwards with wavelength, while in the spatially resampled cube, they form straight lines running vertically in the plot and showing only low frequency structures.

Table 1. Photon counts for extrasolar planets.

Telescope diameter	Distance (pc)	Jupiter	Earth	Earth A-band
2-m	1	1.35×10^5	27000	2490
	2	33700	6760	622
	5	5390	1080	100
10-m	1	3.37×10^6	6.76×10^5	62200
	2	8.42×10^5	1.69×10^5	15500
	5	1.35×10^5	27000	2500
30-m	1	3.03×10^7	6.08×10^6	5.6×10^5
	2	7.58×10^6	1.52×10^6	1.4×10^5
	5	1.21×10^6	2.43×10^5	22400
	50	12100	2430	224

Note. — Table computed assuming flux ratios relative to the host star 1.04×10^{-10} and 5.18×10^{-10} for Earth and Jupiter respectively, a Solar count rate of $2.6 \times 10^{10} \text{ sec}^{-1}$ at 1 pc (appropriate to the F814W filter with ACS). The Earth A-band flux, 7580–7800Å was assumed to be 9.2% of the F814W flux. An integration time of 10^4 sec was assumed.